JGR Atmospheres

RESEARCH ARTICLE
10.1029/2023JD039434

Key Points:

- Antarctic atmospheric circulation responds differently to stratospheric aerosol injections that vary by amount and injection latitude(s)
- Changes to the coastal winds impacts surface ice accumulation and shelf ocean temperatures near ice shelves
- Specific injection strategies can slow 21st century ice loss and avoid identified thresholds pertaining to Antarctic tipping points

Supporting Information:

Supporting Information may be found in the online version of this article.

Correspondence to:

P. B. Goddard,
pgoddard@iu.edu

Citation:

Goddard, P. B., Kravitz, B., MacMartin, D. G., Visioni, D., Bednarz, E. M., & Lee, W. R. (2023). Stratospheric aerosol injection can reduce risks to Antarctic ice loss depending on injection location and amount. *Journal of Geophysical Research: Atmospheres*, *128*, e2023JD039434. https://doi.org/10.1029/2023JD039434

Received 9 JUN 2023
Accepted 23 OCT 2023

Author Contributions:

Conceptualization: P. B. Goddard, B. Kravitz, D. G. MacMartin, D. Visioni, E. M. Bednarz
Formal analysis: P. B. Goddard
Funding acquisition: B. Kravitz, D. G. MacMartin
Methodology: P. B. Goddard, B. Kravitz, D. G. MacMartin, D. Visioni, E. M. Bednarz
Project Administration: B. Kravitz, D. G. MacMartin
Supervision: B. Kravitz, D. G. MacMartin
Writing – original draft: P. B. Goddard
Writing – review & editing: P. B. Goddard, B. Kravitz, D. G. MacMartin, D. Visioni, E. M. Bednarz

Stratospheric Aerosol Injection Can Reduce Risks to Antarctic Ice Loss Depending on Injection Location and Amount

P. B. Goddard[1], B. Kravitz[1,2], D. G. MacMartin[3], D. Visioni[4], E. M. Bednarz[3,5,6], and W. R. Lee[3,7]

[1]Indiana University, Bloomington, IN, USA, [2]Pacific Northwest National Laboratory, Richland, WS, USA, [3]Sibley School of Mechanical and Aerospace Engineering, Cornell University, Ithaca, NY, USA, [4]Department of Earth and Atmospheric Sciences, Cornell University, Ithaca, NY, USA, [5]CIRES, University of Colorado, Boulder, CO, USA, [6]NOAA Chemical Sciences Laboratory, Boulder, CO, USA, [7]Climate and Global Dynamics Division, National Center for Atmospheric Research, Boulder, CO, USA

Abstract Owing to increasing greenhouse gas emissions, the Antarctic Ice Sheet is vulnerable to rapid ice loss in the upcoming decades and centuries. This study examines the effectiveness of using stratospheric aerosol injection (SAI) that minimizes global mean temperature (GMT) change to slow projected 21st century Antarctic ice loss. We simulate 11 different SAI cases which vary by the latitudinal location(s) and the amount(s) of the injection(s) to examine the climatic response near Antarctica in each case as compared to the reference climate at the turn of the last century. We demonstrate that injecting at a single latitude in the northern hemisphere or at the Equator increases Antarctic shelf ocean temperatures pertinent to ice shelf basal melt, while injecting only in the southern hemisphere minimizes this temperature change. We use these results to analyze the results of more complex multi-latitude injection strategies that maintain GMT at or below 1.5°C above the pre-industrial. All these multi-latitude cases will slow Antarctic ice loss relative to the mid-to-late 21st century SSP2-4.5 emissions pathway. Yet, to avoid a GMT threshold estimated by previous studies pertaining to rapid West Antarctic ice loss (1.5°C above the pre-industrial GMT, though large uncertainty), our study suggests SAI would need to cool about 1.0°C below this threshold and predominately inject at low southern hemisphere latitudes (~15°S - 30°S). These results highlight the complexity of factors impacting the Antarctic response to SAI and the critical role of the injection strategy in preventing future ice loss.

Plain Language Summary Large portions of the Antarctic ice sheet are imminently vulnerable to melting as global temperatures rise over the 21st century. This melt would lead to consequential sea level rise intensifying coastal flooding and causing large economic and ecological costs. One idea to slow global warming and limit such climate risks, is to deliberately cool the planet by placing reflective particles in the atmosphere to deflect sunlight before it warms the Earth's surface. This idea is called stratospheric aerosol injection (SAI). Here, our computer simulations show that Antarctic ice loss can be slowed by using SAI, however, the results depend on the location of the aerosol injection (Equator, tropics, or high latitudes). We show that putting the particles between 30°N and 30°S with the majority placed in the southern hemisphere has the best potential to slow 21st century Antarctic ice loss in our computer simulations. This study is an example of how various SAI strategies (such as, where to put these particles) can lead to very different regional climate impacts—a result that decision makers must thoroughly consider.

1. Introduction

Solar geoengineering involves the deliberate modification of the Earth's climate system by reflecting sunlight to cool the planet. One example, stratospheric aerosol injection (SAI), would add small, reflective particles into the lower stratosphere to enhance Earth's planetary albedo (Budyko, 1974; Crutzen, 2006). Global climate models are an important tool for the geoengineering research community that allow the analysis of a variety of SAI cases (how much aerosol to inject, at which latitude(s), and during which season(s)) (e.g., Dai et al., 2018; MacMartin et al., 2022; Tilmes et al., 2017; Visioni et al., 2020). These SAI cases are designed to potentially ameliorate some of the negative consequences of climate change, such as global mean temperature (GMT) rise, shifts in precipitation patterns and amount, and Arctic sea ice loss (e.g., Berdahl et al., 2014; Kravitz et al., 2016; Lee et al., 2023; Moore et al., 2014; Tilmes et al., 2013). However, the impact of various SAI cases on the Antarctic region has so far not been extensively studied.

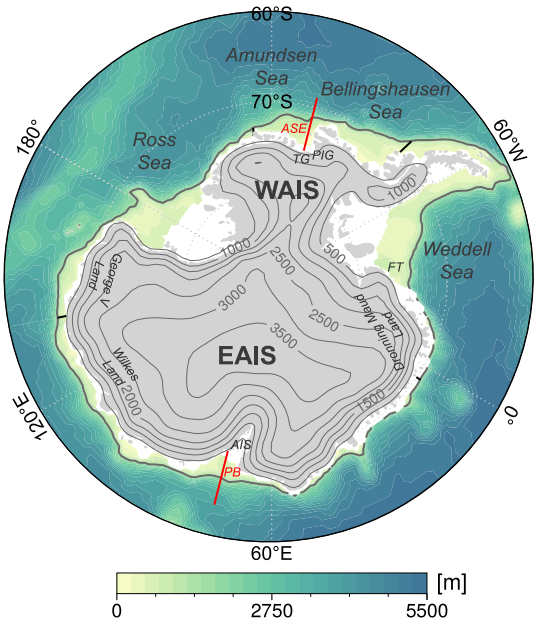

Figure 1. Ocean depth and Antarctic topography map with relevant geographic features labeled. The thick gray contour, representing the 1,500 m isobath, shows the approximate location of the continental shelf break. The thin gray topography contours are at every 500 m. The red lines show the location of cross-shelf ocean profiles in the Amundsen Sea embayment and Prydz Bay analyzed later in the text. The black lines above the shelf waters locate the boundaries of the Amundsen Sea-Bellingshausen Sea sector and the eastern Antarctic sector used in the vertical temperature advection analysis. WAIS, West Antarctic Ice Sheet; EAIS, East Antarctic Ice Sheet; TG, Thwaites Glacier; PIG, Pine Island Glacier; AIS, Amery Ice Shelf; FT, Filchner Trough.

The Antarctic ice sheet is currently losing mass as its marine-terminating glaciers increase in velocity and more rapidly transport ice into the Southern Ocean without a compensating increase in ice accumulation in its interior (Rignot et al., 2019). Ice shelf basal melt rates increase when relatively warm Circumpolar Deep Water (CDW, about 2–4°C above the seawater freezing point (Whitworth et al., 1998)) is transported from the ocean interior onto the continental shelf toward the ice sheet grounding lines, effectively melting the ice shelves from below. In West Antarctica, many of these outlet glaciers rest upon retrograde bedrock which slopes downward inland from the glaciers' grounding lines. At such locations, ice shelf basal melt can detach the glacier at its grounding line whereby eliminating a shelf's buttressing effect and potentially leading to marine ice sheet instability (Hughes, 1973; Schoof, 2007; Weertman, 1974). There is evidence to suggest that this threshold has been passed for several glaciers in West Antarctica (Favier et al., 2014; Joughin et al., 2014; Rignot et al., 2014).

Jacobs et al. (1996) first recognized modified CDW on the continental shelf in the Amundsen Sea embayment (ASE) (Figure 1) near the Pine Island Glacier ice shelf in 1994. Ensuing research has shown that the amount of warm CDW on the continental shelf in this region is sensitive to regional and distal (namely the tropical Pacific) atmospheric variability on interannual to decadal timescales by impacting the coastal easterly wind stress (e.g., Ding et al., 2011; Holland et al., 2019; Thoma et al., 2008). These surface wind stress changes modify the Antarctic Slope Front (ASF) (Jacobs, 1991), which is characterized by downward sloping isopycnals below the surface waters that separate the relatively warm and saline CDW from the cold and fresh shelf seas. The slope of the isopycnals, and thus the strength of the lateral density gradient and barrier between the warm waters and the ice shelves, is largely controlled by the coastal easterly winds (Whitworth et al., 1998). Weaker coastal easterlies decrease Ekman downwelling near the coast, weaken the ASF, and shoal the pycnocline at the shelf break creating a shoreward pathway for CDW transport and the warming of the shelf waters (Spence et al., 2014; Stewart & Thompson, 2015; A. F. Thompson et al., 2014).

In the ASE, coastal wind stress changes are controlled by the strength and position of the Amundsen Sea Low (ASL, Hosking et al., 2013, 2016; Raphael et al., 2016; Turner et al., 2013), which is influenced by the variability in both the Southern Annular Mode (SAM) and in the tropical Pacific sea surface temperatures (e.g., Clem et al., 2017; Ding et al., 2011; Holland et al., 2019; Steig et al., 2012). Notably, as the ASL strengthens (a reduction in sea level pressure (SLP)), easterly winds increase at the shelf break which in turn strengthen the Slope Front and restrict the shoreward CDW transport; conversely, a weak ASL (an increase in SLP) drives anomalous westerly winds at the shelf break which may lead to shelf warming (Dinniman et al., 2011; Donat-Magnin et al., 2017). Furthermore, ASL longitudinal positional shifts will alter zonal winds above the continental shelf with implications for shelf ocean warming. It should also be noted that changes in the strength and position of the cyclonic ASL can drive opposing impacts with regards to the ice shelves in the adjacent Bellingshausen Sea as compared to the Amundsen Sea, as the ASL's center often resides between the two Seas (Figure 1) (Dotto et al., 2020; Verfaillie et al., 2022).

Beyond the Amundsen-Bellingshausen Seas, SAM-related wind anomalies also influence shelf warming across East Antarctica. During the austral summer, positive SAM drives a southward shift of the mid-latitude westerly winds, a weakening of the coastal easterly winds, and a poleward migration of the southern boundary of the Antarctic Circumpolar Current; the latter induces CDW warming at the continental shelf slope, particularly in the Indian Ocean sector of East Antarctica (~110–150°E, Figure 1) (Herraiz-Borreguero & Naveira Garabato, 2022; Yamazaki et al., 2021). This mechanism may be responsible for the increased ice mass loss from this region observed this century (Greenbaum et al., 2015; Rignot et al., 2019; B. Smith et al., 2020). Furthermore, the SAM is projected to become more positive through the 21st century due to continued greenhouse gas emissions (Coburn & Pryor, 2022; Zheng et al., 2013), although an opposing effect from the long-term stratospheric ozone

recovery can significantly offset the positive SAM trend from greenhouse gas emissions, in particularly during the early part of the 21st century and during certain seasons (austral spring and summer, Perlwitz, 2011; D. W. J. Thompson et al., 2011). A positive SAM trend would lead to the Westerlies expanding southward, a weakening of the coastal easterlies, and subsequent Antarctic shelf warming, including warming around East Antarctica (Beadling et al., 2022; Goddard et al., 2017; Spence et al., 2014).

Although the majority of current Antarctic ice mass loss is related to the increased basal melt and calving rates of the ice shelves, surface melt is increasingly becoming a significant contributor to Antarctic mass loss (DeConto & Pollard, 2016; Golledge et al., 2019). By the end of the 21st century, surface melt rates across Antarctica could equal that of Greenland from early this century under the Representative Concentration Pathway 8.5 (RCP8.5) forcing (~600 Gt yr^{-1}; Trusel et al., 2015; van Angelen et al., 2014). Furthermore, increased meltwater on ice shelves may lead to increased hydrofracturing and calving rates (DeConto & Pollard, 2016; Scambos et al., 2009; Trusel et al., 2015). Surface melt rates around the Antarctic periphery have been shown to modulate with phases of SAM and the El Niño Southern Oscillation (ENSO) (e.g., Johnson et al., 2022; Scott et al., 2019). Many ice shelves along East Antarctica (in the Dronning Maud Land, Amery and Wilkes Land, and the Ross Sea sector of West Antarctica, Figure 1) show a negative correlation between melt days and the spring-summer SAM index (Johnson et al., 2022). Whereas melt days for ice shelves along the Amundsen Sea and eastern Ross Sea sector show a positive correlation with the spring-summer ENSO index (Johnson et al., 2022; Scott et al., 2019).

Opposingly, snow accumulation on Antarctica is projected to increase in the 21st century, acting to partially offset the mass loss from increased ocean thermal forcing and surface melt (Payne et al., 2021). Many regions inland from the coast receive a large proportion (~40–60%) of their annual precipitation during infrequent but extreme events characteristic of atmospheric rivers (Davison et al., 2023; Schlosser et al., 2010; Turner et al., 2019; Wille et al., 2021). Over the 21st century atmospheric rivers are projected to increase in duration and strength due to a warmer atmosphere's capacity to hold more moisture (Espinoza et al., 2018; O'Brien et al., 2022; Payne et al., 2020).

Despite the projected increase in Antarctic snow accumulation, under RCP8.5 forcing, sea level rise contributions from Antarctica are projected to increase and to surpass Greenland by the year 2100 (with the upper end of the likely contribution being ~0.3 m above the 1986–2005 mean, though the possibility of such dynamic responses as marine ice sheet instability result in large uncertainty regarding this estimate; IPCC, 2019). Armstong McKay et al. (2022) synthesize numerous observation and modeling studies (e.g., Arthern & Williams, 2017; Feldmann & Levermann, 2015; Garbe et al., 2020; H. Yu et al., 2019) to estimate that the West Antarctic Ice Sheet (WAIS) is susceptible to self-perpetuating collapse if global mean temperatures pass ~1.5°C above pre-industrial levels. It is therefore prudent to research the Antarctic climate response and projected ice loss in SAI cases where global mean warming is kept below 1.5°C.

However, the only previous studies explicitly examining SAI impacts on the Antarctic region, McCusker et al. (2015) and Sutter et al. (2023), largely show that solar geoengineering is unable to prevent Antarctic shelf warming and the eventual collapse of the WAIS. Sutter et al. (2023) results, contingent upon the amount of SAI and the temperature target for GMT, will be addressed at the end of Discussion Section 4.1. McCusker et al. (2015) results, contingent on where (which latitudes) the injection occurs, show that a sulfate aerosol addition between 10°S and 10°N beginning in 2035 will still lead to warming of the subsurface Antarctic shelf waters around the mid-21st century (albeit less warming than the RCP8.5 scenario alone) despite cooling mid-21st century global mean surface air temperature (SAT) to the late-twentieth century level. The authors focus on the ASE and attribute the persistent shelf ocean warming at depth to the equatorial sulfate injection disrupting the upper troposphere/lower stratosphere meridional temperature gradients, thereby leading to a weakening of the coastal easterlies and increased Ekman upwelling of the relatively warm CDW onto the shelf.

Using a similar climate model, Bednarz et al. (2022) shows that while deploying SAI at the Equator or in the northern hemisphere does indeed simulate induce similar weakening of the coastal easterlies as found in McCusker et al. (2015), injecting in the southern hemisphere will strengthen coastal easterlies relative to a mid-century SSP2-4.5 scenario. Specifically, Bednarz et al. (2022) finds that injecting SO_2 at the Equator, 15°N, or 30°N will shift the southern hemisphere tropospheric eddy-driven jet poleward resulting in SLP and wind patterns consistent with a positive phase of SAM, while injecting at 15° or 30°S will shift the eddy-driven jet equatorward resulting in patterns consistent with a negative phase SAM. This opposing impact of SAI on Antarctic regional atmospheric conditions and circulation with respect to the hemisphere of aerosol injection motivates the current

Table 1
A Summary of the Eleven Stratospheric Aerosol Injection Simulations and the Historical and SSP2-4.5 Simulations Including the Number of Ensemble Members, Latitude(s) of Injection, the Season(s) or Year-Round Application of the Injection, the Approximate Amount of Injection Averaged During 2050–2069 in Tg-SO_2 yr^{-1}, the Analysis Time Period, and the Global Mean Temperature Response During This Time Period Relative to the Pre-Industrial Time Period (±1 Standard Error, Where the Sample Size is the Number of Years Across All Ensemble Members)

Sim. Abbr.	Ens. Mem.	Latitude of inj.	Ann. or Seas.	Tg-SO_2 yr^{-1}	Analysis	GMT—PI (°C)
HIST	3	N/A	N/A	N/A	1990–2009	0.6 ± 0.1
SSP2-4.5	3	N/A	N/A	N/A	2050–2069	2.4 ± 0.1
30N-ANN	2	30°N	ANN	12.0	2050–2069	1.4 ± 0.1
15N-ANN	2	15°N	ANN	12.0	2050–2069	1.5 ± 0.1
EQ-ANN	2	Equator	ANN	12.0	2050–2069	1.6 ± 0.1
15S-ANN	2	15°S	ANN	12.0	2050–2069	1.4 ± 0.1
30S-ANN	2	30°S	ANN	12.0	2050–2069	1.3 ± 0.1
60S-SON	1	60°S	SON	12.0	2050–2069	1.6 ± 0.1
60N-MAM	1	60°N	MAM	12.0	2050–2069	1.7 ± 0.1
Global+1.5	3	30°N, 15°N, 15°S, 30°S	ANN	8.6	2050–2069	1.6 ± 0.1
Global+1.0	3	30°N, 15°N, 15°S, 30°S	ANN	17.0	2050–2069	1.0 ± 0.1
Global+0.5	3	30°N, 15°N, 15°S, 30°S	ANN	25.6	2050–2069	0.6 ± 0.1
Polar+1.0	3	60°N, 60°S	MAM, SON	20.4	2050–2069	1.2 ± 0.1

Note. The simulation name is in *italics* if their results are located in Supporting Information S1.

study. Here we use a comprehensive set of seven single-latitude injection sensitivity simulations and four more complex multiple-latitude injection cases to systematically analyze the following questions: How do various SAI cases impact the SAM and ASL variability (Section 3.1)? Which SAI cases lead to warmer SAT or greater precipitation above the continent relevant to surface mass balance (Sections 3.1 and 4.1)? Finally, which SAI cases lead to continued upwelling of warm water on the Antarctic continental shelf (Sections 3.2 and 4.1)?

2. Model and Methods

In this work we consider 11 SAI cases (Table 1) simulated using the Community Earth System Model version 2, using the Whole Atmosphere Community Climate Model version 6 as the atmospheric component (CESM2-WACCM6; Danabasoglu et al., 2020; Gettelman et al., 2019). The atmospheric horizontal resolution is 1.25° longitude by 0.95° latitude, with 70 vertical layers extending from the surface to about 140 km. The simulations use the Middle Atmosphere chemistry configuration (Davis et al., 2022) that includes an interactive stratospheric and upper atmospheric chemistry in addition to aerosol microphysics from the Modal Aerosol Module (MAM4; Liu et al., 2016). The ocean model (Parallel Ocean Program Version 2) horizontal resolution is 1.125° in the zonal direction and ranges between about 0.27° and 0.64° in the meridional direction and includes 60 vertical levels (Danabasoglu et al., 2012; R. Smith et al., 2010). There is not a coupled dynamic Antarctic ice sheet model in our simulations and as such sub ice shelf melt is not represented. However, here we use the continental shelf seas (referred to in this text as the shelf ocean) warming to represent basal melt potential. The simulations use the coupled Land Model version 5.0 (Lawrence et al., 2019) to track surface ice mass balance. Mass loss due to calving is not simulated. Each SAI case is simulated using the background CMIP6 SSP2-4.5 scenario (Meinshausen et al., 2020) with the sulfate precursor (SO_2) injection beginning in January 2035 and continuing through December 2069.

The first set of SAI cases, consisting of seven simulation setups, each inject SO_2 at every timestep at a single latitude into the lower stratosphere at a constant rate equivalent to 12 Tg-SO_2 per year (Table 1). The first five of these simulations, which inject SO_2 year-round at ∼21.5 km altitude and either at 30°N, 15°N, 0°N, 15°S, or 30°S, respectively, were introduced in Visioni et al. (2023) and Bednarz et al. (2023) and used to examine the response of the SAM to SAI in Bednarz et al. (2022). Additionally, we introduce two other single-latitude injection cases that inject at 60°S during the austral spring (SON) or at 60°N during the boreal spring (MAM) at about

15 km in altitude. At these high latitudes, injections are proposed in the Spring to account for the seasonal cycle of insolation and the relatively shorter lifetime of aerosols in the stratosphere at these latitudes (Lee et al., 2021). This method would ensure that aerosol concentrations are low during winter and at the beginning of spring, when sunlight-driven heterogeneous chemistry would result in increased ozone depletion. These six SAI cases are abbreviated as 60N-MAM, 30N-ANN, 15N-ANN, EQ-ANN, 15S-ANN, 30S-ANN, and 60S-SON.

The second set of SAI cases, consisting of four more complex simulation setups, each inject SO_2 at every time-step at multiple latitudes simultaneously and under time-varying injection rates (Table 1). The injection rates are determined at the beginning of each year by a feedback algorithm such as to maintain the annual global mean near-surface temperature (GMT) at a chosen level above the pre-industrial (PI) conditions. Three of these simulations, introduced in MacMartin et al. (2022), each inject at 30°N, 15°N, 15°S, and 30°S to maintain GMT at 1.5°C + PI, 1.0°C + PI, and 0.5°C + PI, respectively. After slowly increasing SAI rates to meet the GMT goals, the GMT for years 2050–2069 in these simulations have the same GMT as years 2020–2039, 2008–2027, and 1993–2012 from the CESM2-WACCM6 SSP2-4.5 and/or historical forcing simulations, respectively. These SAI cases also meet two other objectives: maintaining the interhemispheric surface temperature gradient and the Equator-to-pole surface temperature gradient at their reference PI levels as detailed in Kravitz et al. (2017) and Tilmes et al. (2018). Additionally, we introduce a fourth multi-latitude injection case that injects at 60°S during austral Spring (SON) and 60°N during boreal Spring (MAM) to meet the 1.0°C + PI GMT objective (Zhang et al., 2023). These four SAI cases are abbreviated as Global+1.5, Global+1.0, Global+0.5, and Polar+1.0. For these cases, the total amount of SO_2 injected per year averaged for years 2050–2069 is about 8.6, 17.0, 25.6, and 20.4 Tg-SO_2 yr^{-1}, respectively (Visioni et al., 2023; Zhang et al., 2023).

The two different sets of SAI cases serve two complementary purposes. The single-latitude injection cases, with a fixed amount injected per year, serve to more easily diagnose changes to the climate system by considering one location at a time. Their purpose is not to illustrate a desirable deployment strategy; rather, they serve as a "step-function" response which can inform more complex strategies that rely on a combination of multiple injection locations and use time-varying injection rates to maintain one or more climate targets, assuming a certain linearity of the system and additivity between different locations (Visioni et al., 2023). Bednarz et al. (2022) showed the potential of these single-latitude injection simulations to explore physical mechanisms driving the SAI responses and to explain changes in another set of multi-latitude injection simulations for one particular climate driver, the SAM. Finally, comparisons between the Global+1.5, Global+1.0, Global+0.5 simulations allow one to ascertain to which degree the observed changes depend on the amount of GMT cooling obtained, while comparisons between Global+1.0 and Polar+1.0 allow a comparison of two strategies with similar GMT, but different injection strategies. All 11 SAI cases are summarized in Table 1, including the number of ensemble members for each strategy.

Here, we analyze the ensemble mean results from the last 20 years of the SAI simulations (2050–2069) and compare them to CESM2-WACCM6 simulations of the CMIP6 historical forcing near the turn of the 21st century (1990–2009). We contrast these responses with the analogous responses simulated in the CESM2-WAACM6 CMIP6 SSP2-4.5 simulations as a control greenhouse gas scenario without SAI for the same time period (2050–2069). In the Discussion Section 4.1, we also compare the SAI simulations (2050–2069) to the time period when the GMT is 1.5°C above the pre-industrial in the SSP2-4.5 scenario (years 2020–2039). We denote a statistically significant change where the difference in the two means is greater than ±2 standard errors. The sample size is the number of years across all ensemble members and is adjusted depending upon the autocorrelation at each model grid box, where necessary (Wilks, 1997).

3. Results

3.1. Antarctic Surface Climate

In addition to reflecting incoming solar radiation, the injected aerosols will also absorb outgoing terrestrial radiation and some incoming solar radiation which in turn warms the lower stratosphere. This localized warming with respect to the Historical simulation (1990–2009) is shown in the first two columns of Figure 2. Consistent with the results of Bednarz et al. (2022), who use the same single-latitude SAI simulations, this warming strengthens the stratospheric Equator-to-pole temperature gradient initiating a year-round strengthening of the stratospheric polar jet (Figure 2—last column). This dynamical response also alters tropospheric circulation expressed through

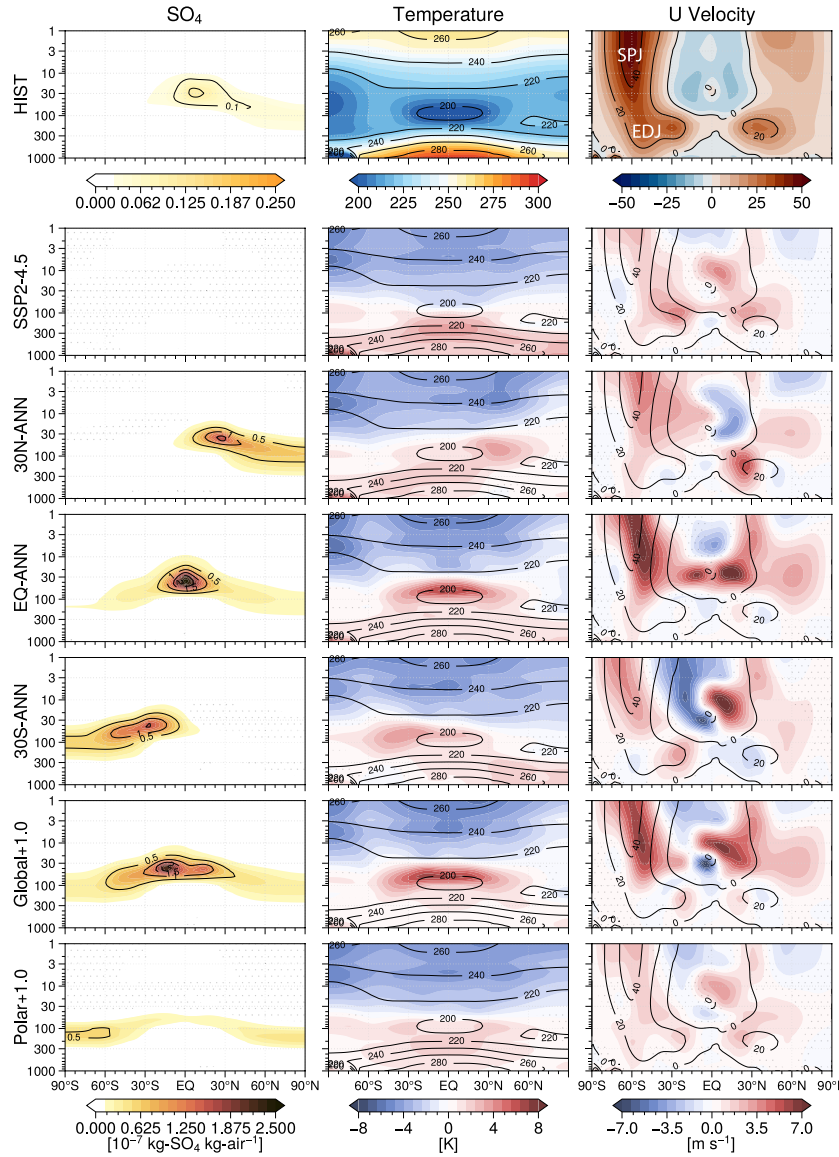

Figure 2. The top row shows the Historical annual ensemble mean (1990–2009) zonal mean sulfate burden (10^{-7} kg-SO_4 kg-air^{-1}), temperature (K), and zonal wind velocity (m s^{-1}). Shading in the following rows show the annual ensemble mean anomalies (2050–2069) from the Historical with respect to SSP2-4.5 and the stratospheric aerosol injection cases. Contours in the first column show the sulfate burden difference from the Historical, whereas, in columns two and three, contours show the corresponding temperatures and zonal velocity in the Historical simulation for reference. Stippling shows the regions where the difference is not statistically significant. SPJ = southern hemisphere stratospheric polar jet; EDJ = southern hemisphere eddy-driven jet.

latitudinal shifts and/or strength modification of the tropospheric eddy-driven jet. Of particular importance to the current study, in the southern hemisphere (SH) these anomalies differ in sign and magnitude depending on the latitude(s) of the injection. The single-latitude injection cases at the Equator (EQ-ANN), 15°N (15N-ANN, Figure S1 in Supporting Information S1), or 30°N (30N-ANN) shift the SH eddy driven jet poleward, whereas injection cases at 15°S (15S-ANN, Figure S1 in Supporting Information S1) or 30°S (30S-ANN) shift the tropospheric jet Equatorward. Furthermore, these circulation anomalies reach the surface at about 60°S and are expressed as westerly anomalies for the Equator and northern hemisphere (NH) injection cases and easterly anomalies (or no significant change) for SH injection cases. As described in Bednarz et al. (2022) these opposite responses at the surface are linked to associated changes in the tropospheric eddy heat and momentum fluxes as well as stratospheric wave propagation or breaking and high latitude downwelling during austral winter and spring.

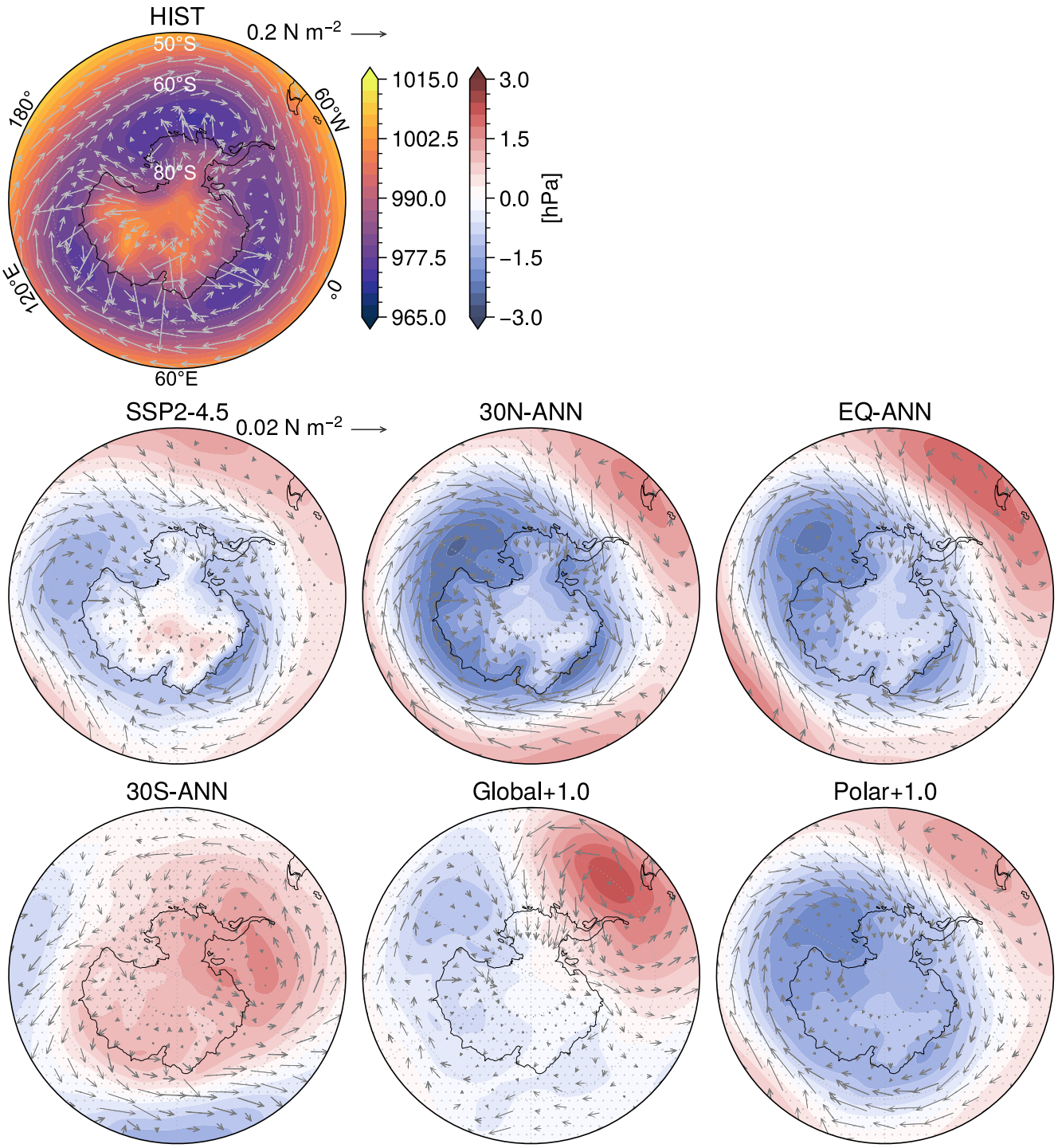

Figure 3. The top left panel shows the Historical annual ensemble mean (1990–2009) sea level pressure (SLP) (hPa) and surface wind stress vectors (N m^{-2}, in the direction of the surface winds). The following rows show the annual ensemble mean anomalies (2050–2069) from the Historical with respect to SSP2-4.5 and the stratospheric aerosol injection cases. Stippling shows the regions where the SLP difference is not statistically significant.

The single-latitude injection cases also reveal that the Equator and NH single-latitude injections drive year-round SLP reductions above Antarctica and westerly surface wind stress anomalies around the coastline consistent with a positive phase of SAM (Figure 3 and Figure S2 in Supporting Information S1). These anomalies are similar in pattern and larger in magnitude as compared to the SSP2-4.5 anomalies which also reflect a positive SAM and are consistent with previous studies projecting a positive trending SAM through the 21st century under

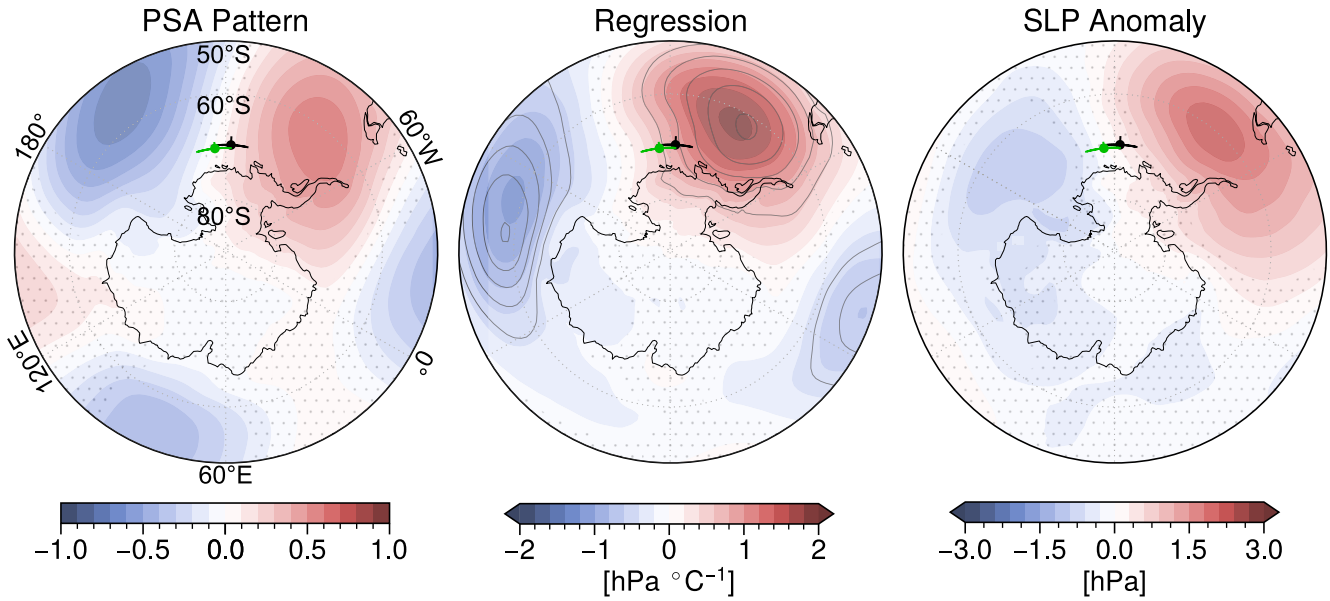

Figure 4. The left panel shows the Pacific-South American (PSA) pattern defined from the standardized leading modes of variability from an empirical orthogonal function analysis of the Historical (1990–2009) area-weighted monthly mean sea level pressure (SLP) anomalies with respect to its climatology poleward of 20°S (L. Yu et al., 2012). The pattern shown accounts for 11.4% ± 0.2% (±1 standard deviation with respect to the ensemble members) of the variability in the anomalous SLP field (the Southern Annular Mode pattern accounts for 26.5% ± 1.8% and the other PSA pattern (associated with sea surface temperature in the tropical Pacific but best correlates with the depth of the Amundsen Sea Low (ASL)) accounts for 9.4% ± 0.7%). The center panel shows the linear regression slope of Global+1.0 (2050–2069) monthly SLP anomalies from the Historical onto the Global+1.0 monthly central Pacific (5°S:5°N & 160°E:30°W average) sea surface temperature anomalies from the Historical. The contours show the explained variance (contours begin at 5% and increase by 5% per level). The right panel shows the annual ensemble mean anomalies of Global+1.0 from the Historical ensemble mean SLP (hPa). In all panels, the center of the green cross marks the annual mean location of the Historical ASL position, and the black cross marks the Global+1.0 ASL position, with ±1 standard deviation in the longitudinal and latitudinal directions (crosses). Stippling shows the regions where the values are not statistically significant.

greenhouse gas forcing (Coburn & Pryor, 2022; Zheng et al., 2013). Conversely, SH single-latitude injections drive anomaly fields consistent with a negative SAM (pressure increases and easterly wind anomalies above and around Antarctica).

Analyzing the surface wind stress and SLP anomalies resulting from the single-latitude injection cases can help interpret the results from the multi-latitude injection cases: Global+1.0 and Polar+1.0 (with Global+0.5 and Global+1.5 shown in Supporting Information S1). The Global+1.0 case shows that the westerly anomalies derived from the stratospheric polar jet strengthening do not propagate down to the troposphere and modify the tropospheric jet nor drive westerly anomalies at the surface at 60°S (Figure 2—last column). Therefore, the circumpolar wind stress and SLP anomalies do not reflect a characteristic positive SAM phase that one would expect under the strengthening of the stratospheric jet (Figure 3). Instead, the anomalous SLP dipole off the coast of West Antarctica and the Peninsula is consistent with the Pacific-South American (PSA) pattern that represents an Equator-to-pole atmospheric Rossby wave response to changes in central tropical Pacific sea surface temperature (Kidson, 1998; Mo & Higgins, 1998; Yueng et al., 2019).

This PSA pattern accounts for 11.4% ± 0.2% (±1 standard deviation with respect to the ensemble members) of the variability in the anomalous SLP field and is associated with longitudinal shifts in the ASL wherein positive central Pacific sea surface temperature anomalies are associated with a blocking high over the Antarctic Peninsula and a westward migration of the ASL (Figure 4). (The SAM pattern accounts for 26.5% ± 1.8% and the other PSA pattern, also associated with sea surface temperature in the tropical Pacific but best correlates with the depth of the ASL due to a 90° zonal phase shift from the other PSA mode, accounts for 9.4% ± 0.7%). These PSA patterns have been shown to impact the ASL position and depth from seasonal to decadal timescales (e.g., Ding et al., 2011; Goddard et al., 2021; Holland et al., 2019; Kidson, 1998). In this study, we will focus on the PSA pattern that is associated with ASL longitudinal shifts and is reflected in the anomalous SLP patterns in Global+1.0 (Figure 3). This PSA teleconnection is less prominent for SAI cases that strengthen the SH eddy-driven jet as this frontal enhancement reflects or breaks the Rossby wave train before reaching the Amundsen-Bellingshausen Seas region (Schneider et al., 2012; Yueng et al., 2019).

The Polar+1.0 surface wind stress and SLP anomalies can also be interpreted through the analysis of the single-latitude injection simulations. Both 30S-ANN (significant change) and 15S-ANN (non-significant) show easterly anomalies in the annual zonal mean velocity at the surface at 60°S (Figure 2 and Figure S1 in Supporting Information S1). However, in 60S-SON this anomaly is weakly westerly (non-significant, Figure S1 in Supporting Information S1). This anomaly is, at least in part, due to the preferential cooling of the SH high latitudes and relative warming of the mid-to-low latitudes which enhances the tropospheric meridional temperature gradient and results in increased westerly winds at the surface. Furthermore, in addition to injecting at 60°S in austral spring, the Polar+1.0 simulation also injects at 60°N in boreal spring (MAM). Consistent with the 15N-ANN and 30N-ANN responses, 60N-MAM strengthens the tropospheric polar jet resulting in significant westerly wind anomalies at the surface near 60°S (Figures S1 and S2 in Supporting Information S1). Therefore, the combination of injecting at both 60°S and 60°N as the Polar+1.0 case does, results in a significant annual mean westerly anomaly at the surface at 60°S (Figure 2). The surface wind stress and SLP anomaly fields are in turn consistent with a positive SAM (Figure 3). In summary, both Global+1.0 and Polar+1.0 similarly reduce GMT relative to the pre-industrial while the different injection distribution drives different dynamical responses that lead to different circulation patterns around Antarctica.

For each SAI case, the simulated atmospheric circulation changes will drive SAT and precipitation anomalies around Antarctica. To first order these anomalies respond to hemispheric-scale temperature changes that differ with respect to each SAI case. The annual mean change in SAT poleward of 50°S with respect to the Historical simulation is +1.7° (SSP2-4.5), +1.5° (30N-ANN), +1.0° (EQ-ANN), −0.2° (30S-ANN), +0.4° (Global+1.0), and +0.3°C (Polar+1.0), where one standard error of the difference in means is about 0.05°C. (For context, the corresponding temperature in years 2008–2027 from the SSP2-4.5 simulation where the GMT was the same as in Global+1.0 and Polar+1.0 was +0.4°C; the polar strategy indeed focuses more cooling on the high-latitude regions relative to the global mean.) As expected, the cases which inject the least SO_2 in the SH cool SAT in the Antarctic region the least, leaving residual warming as the impact of increasing greenhouse gases is not being fully offset (Figure 5). Consistent across all cases except for 30S-ANN and 60S-SON (Figure S3 in Supporting Information S1), the positive SAT anomalies over the ocean are greatest across the eastern Amundsen Sea to the Antarctic Peninsula and between about 20°E and 50°E. These locations are associated with wind anomalies that have a northerly component which not only transports warmer air from lower latitudes to the area but also contributes to the reduced local sea ice extent (Figure 5—contours). Regarding each case, SAT anomalies over the continent vary less than the anomalies over the nearby ocean, with the largest residual warming relative to the Historical typically located on the Antarctic Peninsula and over West Antarctica.

Similarly, the simulated total precipitation anomalies over Antarctica are primarily associated with the changing moisture capacity of the atmosphere. The annual mean 50°S-to-pole total precipitable water anomaly with respect to the historical simulation is +1.0 (SSP2-4.5), +0.8 (30N-ANN), +0.6 (EQ-ANN), −0.1 (30S-ANN), +0.2 (Global+1.0), and +0.3 kg m^{-2} (Polar+1.0), where one standard error of the difference in means is about 0.03 kg m^{-2} (Figure 6—contours). Superimposed upon these mean changes in total precipitable water, the circulation anomalies drive significant regional increases in precipitation along the coast of West Antarctica, the Peninsula, and between about 0° and 60°E in East Antarctica (Figure 6 and Figure S4 in Supporting Information S1). The positive precipitation anomaly toward the tip of the Peninsula and between 0° and 60°E in the Equator, NH, and Polar+1.0 cases is due to the westerly storm track migrating southward associated with the positive SAM conditions (Wille et al., 2021), whereas, the precipitation increase in West Antarctica is due to the westward migration of the ASL and the positive pressure anomaly near the Peninsula associated with the PSA pattern (Figure 3) (Adusumilli et al., 2021; Maclennan & Lenaerts, 2021). These PSA-associated SLP anomalies are most prominent in Global+1.0 and set up a moisture pathway from the lower latitudes to the interior of West Antarctica (a similar response is found in Global+1.5 and Global+1.0, Figures S2 and S4 in Supporting Information S1). In the SH single-latitude injection cases, changes to precipitation around the Antarctic periphery are very small and often non-significant.

Combining the changes to SAT and precipitation over Antarctica, we can assess simulated changes to surface ice accumulation for each SAI case. In the Historical simulation, only at the northern tip of the Peninsula is the amount of surface ice melt greater than ice formation resulting from precipitation (Figure 7). Across the rest of Antarctica there is an annual mean gain in surface ice mass. With respect to the Historical, the SAI surface accumulation anomalies are very similar to the anomalous precipitation patterns (Figures 6 and 7; Figures S4 and S5 in Supporting Information S1). The enhanced hydrological process dominates the mass gain anomalies because despite SAT increase for most SAI cases, the temperature is still below 0°C for the annual mean (Figure 5 and Figure S3 in Supporting Information S1). The only exception under most SAI cases is at the northern part of the

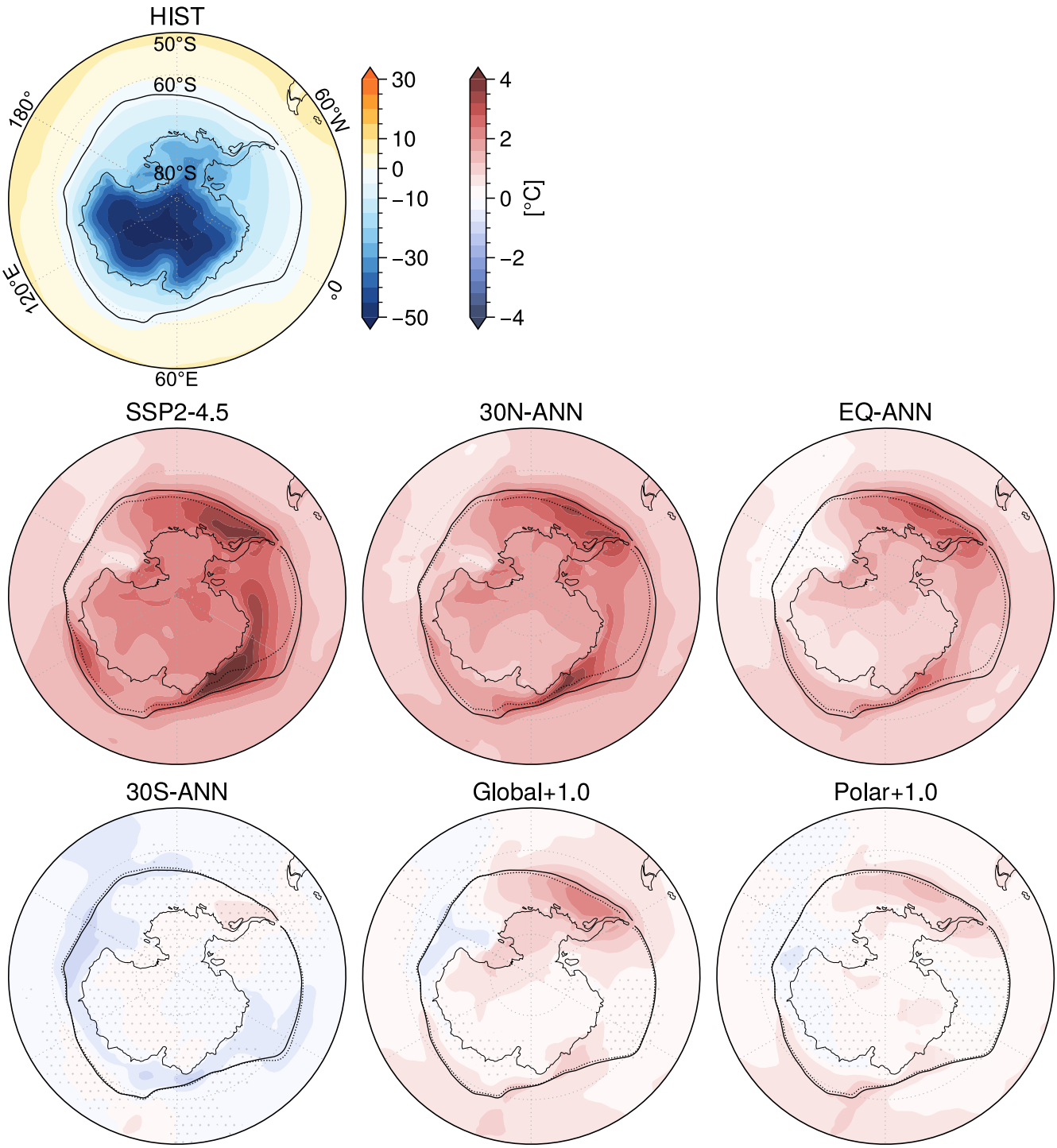

Figure 5. The top left panel shows the Historical annual ensemble mean (1990–2009) surface air temperature (SAT, °C) with a solid black contour showing the sea ice extent (at 25% concentration). Shading in the following rows show the annual ensemble mean SAT anomalies (2050–2069) from the Historical with respect to SSP2-4.5 and the stratospheric aerosol injection (SAI) cases. Each of these panels show the Historical sea ice extent contour (solid) and the SSP2-4.5 or SAI case contour (dashed). Stippling shows the regions where the SAT difference is not statistically significant.

Peninsula where the SAT increases and ice formation declines relative to the Historical. The reduction in ice accumulation at this location can exceed −2.0 mm day^{-1}. Furthermore, consistent with the precipitation results, the SH single-latitude injection cases show small, and often non-significant changes to ice accumulation. In summary, the surface ice accumulation anomalies shown in the NH single-latitude or multi-latitude SAI cases with

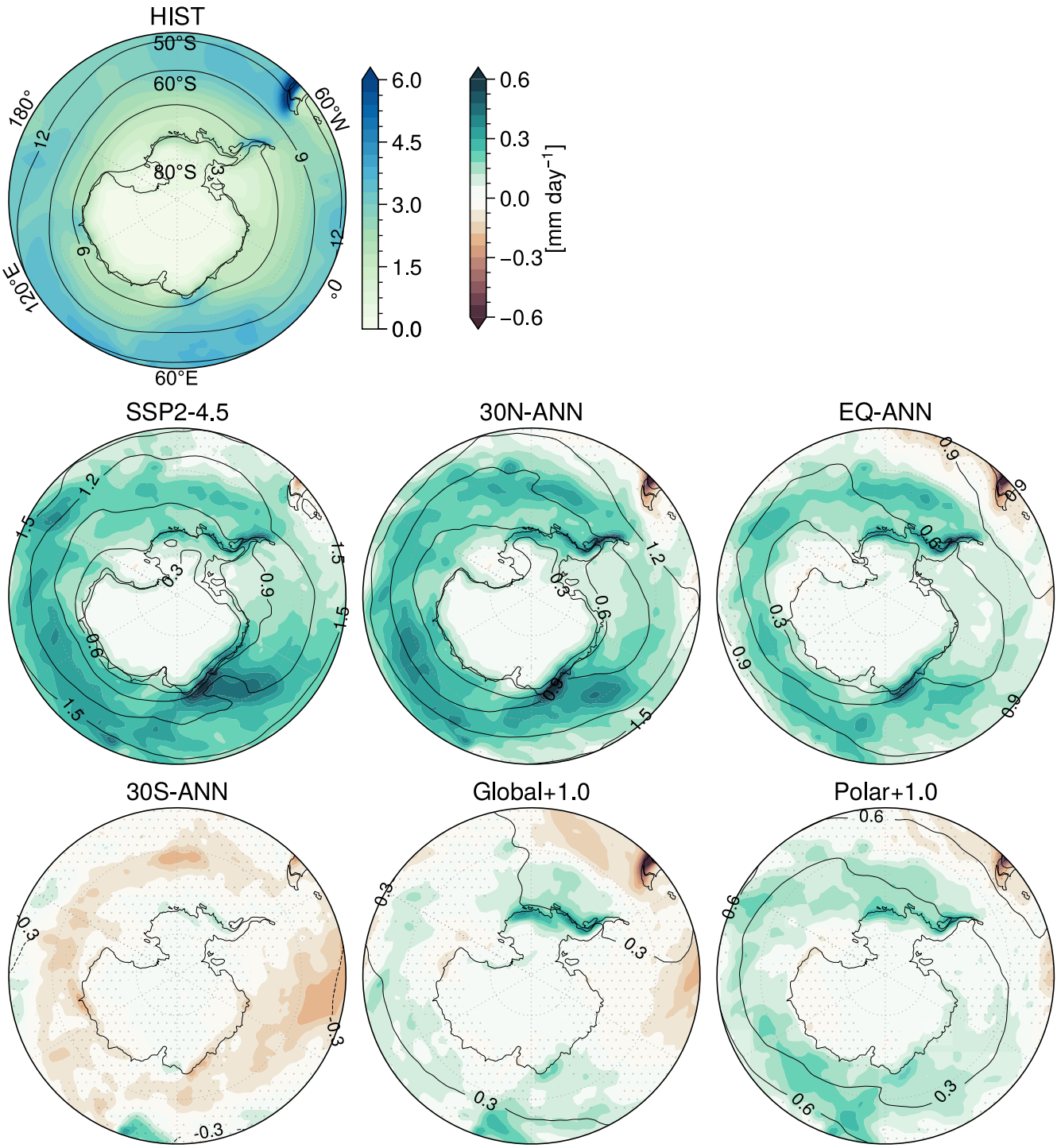

Figure 6. The top left panel shows the Historical annual ensemble mean (1990–2009) total precipitation (mm yr^{-1}) with black contours showing total precipitable water (kg m^{-2}). Shading in the following rows show the annual ensemble mean total precipitation anomalies with black contours showing total precipitable water anomalies (2050–2069) from the Historical with respect to SSP2-4.5 and the stratospheric aerosol injection cases. Stippling shows the regions where the total precipitation difference is not statistically significant.

respect to the Historical simulation are largely driven by precipitation increases. These precipitation increases are due to the enhanced hydrological cycle from the background greenhouse warming relative to the Historical that is not completely offset by these SAI cases (Visioni et al., 2023). Moreover, the regional ice accumulation variability is consistent with changes to the SAM index or longitudinal shifts of the ASL via the PSA teleconnection.

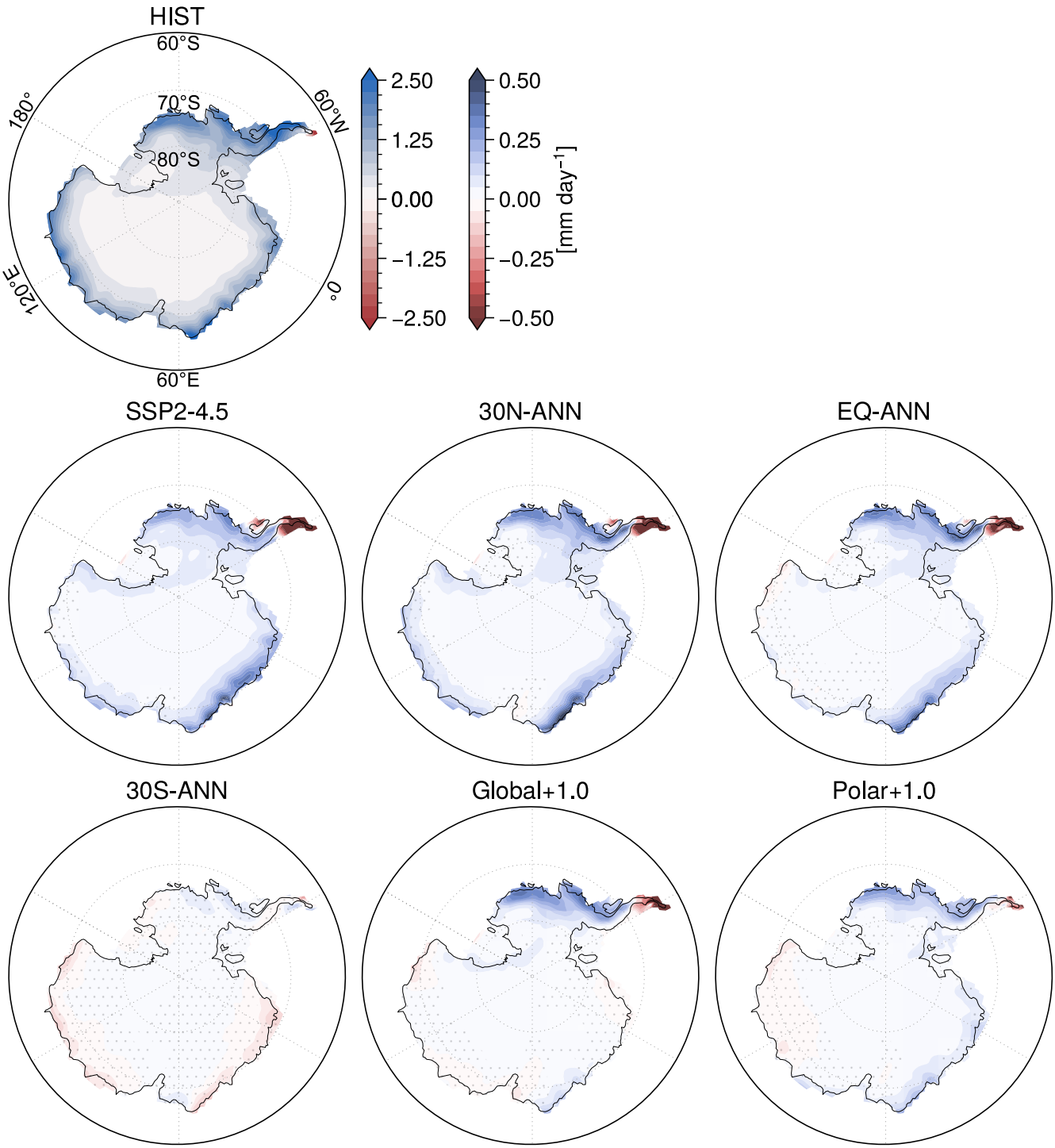

Figure 7. The top left panel shows the Historical annual ensemble mean (1990–2009) net surface ice accumulation (mm day^{-1}). Shading in the following rows show the annual ensemble mean ice accumulation anomalies (2050–2069) from the Historical with respect to SSP2-4.5 and the stratospheric aerosol injection cases. Stippling shows the regions where the accumulation difference is not statistically significant.

3.2. Antarctic Shelf Ocean

The Antarctic surface climate anomalies directly alter ocean conditions above the continental shelf through three surface mechanisms: surface ocean radiative flux, surface ocean momentum flux through wind stress, and surface ocean salinity flux. With regards to the first mechanism, Figure S6 in Supporting Information S1 shows that the

largest near surface shelf ocean temperature warming (0–100 m mean) occurs near the Peninsula and along East Antarctica between about 20°E and 50°E coinciding with positive SAT temperature anomalies over these regions as shown in Figure 5 and Figure S3 in Supporting Information S1. Similarly, these 0–100 m mean shelf ocean temperature anomalies are primarily driven by the mean large (hemispheric) scale SAT anomalies and the surface radiative flux response due to shifts in the SAM index. Furthermore, like the SAT anomalies, the Equator and NH single-latitude SAI cases warm these surface waters the most and the SH-only, Global+1.0, and Polar+1.0 SAI cases show minimal warming (and sometimes even significant cooling) with respect to the Historical.

Shelf ocean warming below 100 m, pertinent to ice shelf basal melt and ice sheet mass loss, is primarily driven by surface wind stress changes near Antarctica's coastline. A change to the wind stress curl, or Ekman pumping, impacts the downwelling rate of the surface waters at the ocean-ice shelf interface. When coastal easterly wind stress is robust, Ekman pumping continuously supplies cold fresh surface waters to the subsurface of the shelf ocean. However, when easterly wind stress weakens there is anomalous Ekman upwelling of the off-shelf relatively warm and saline CDW onto the shelf where it warms the surrounding shelf waters from below. Figure 8 and Figure S7 in Supporting Information S1 show that the Historical Ekman downwelling is significantly reduced (a relative Ekman upwelling anomaly) along most of the West Antarctic and East Antarctic coastline for the Equator and the NH-only SAI cases as well as SSP2-4.5. The Ekman upwelling anomalies for Global+1.0 and Polar+1.0 are comparatively lower in magnitude or non-significant in these regions. Moreover, the 30S-ANN SAI cases increases Ekman pumping along East Antarctica and the western portion of West Antarctica as a result of the increased coastal easterly wind stress, as explained in the previous Results Section and shown in Figure 3. For each respective SAI case, these simulated changes to Ekman pumping are consistent with the associated impacts on the SAM and the resulting surface wind stress anomalies along the coast.

Comparing the anomalous Ekman pumping patterns to the 100–1,000 m mean shelf ocean temperature anomalies reveals a qualitative link between changes in the surface wind stress and the subsurface shelf ocean temperature (Figure 9 and Figure S8 in Supporting Information S1). In general, for the Equator and NH SAI cases and at the locations for which coastal Ekman upwelling anomalies occur, the mean subsurface shelf ocean temperature increases; and opposingly, for the SH SAI cases and locations where Ekman downwelling is enhanced, the mean subsurface temperature decreases relative to the Historical. An exception to this generalization is the 100–1,000 m mean shelf ocean warming simulated in all SAI cases in the Weddell Sea sector. The simulated Weddell Sea shelf warming is likely associated with the interaction between the Filchner trough (see Figure 1) and the ASF and Current which reside just offshore of the shelf break (Hellmer et al., 2012). The shoaling of the isopycnals in the ASF near the Filchner trough in response to temperature, salinity, or wind stress changes can initiate a pathway for off-shelf CDW to encroach upon the shelf (Bull et al., 2021; Ryan et al., 2020). However, in a regional high-resolution modeling study, Daae et al. (2020) shows that relatively severe changes to the ASF would need to occur for the warm water to consistently access the Weddell Sea shelf. Therefore, in the current study, it is likely that the Weddell Sea shelf ocean warming is an overestimate given that this response results in all SAI cases despite opposing changes to surface wind stress and that many of the relevant processes occur at the subgrid scale and are thus parameterized in the current simulations. Caveats concerning the ocean model's resolution are further explained in the Discussion section.

To further analyze the drivers of subsurface shelf warming we now focus on regions where evidences of CDW (or modified CDW) have been observed: near the ice shelves in the Amundsen Sea (Jacobs et al., 1996), the Bellingshausen Sea (Jenkins & Jacobs, 2008), and around East Antarctica near the Totten Glacier (~116°E) (Greenbaum et al., 2015), Vincennes Bay (~110°E) (Ribeiro et al., 2021), and Prydz Bay (PB) (~74°E) (Herraiz-Borreguero et al., 2015). To do so, we create a depth profile above the shelf and landward of the shelf break of vertical temperature advection averaged across the Amundsen-Bellingshausen Seas (ASBS) from 75°W—130°W and in East Antarctica (EAIS) from 5° to 140°E (see Figure 1 for these shelf boundary locations). Furthermore, we analyze cross-shelf transects of potential temperature, salinity, and potential density that are representative of these regions at 106°W (ASE) and at 74°E (PB, see Figure 1 for these transect locations). It is essential to recognize that the following results come with caveats and limitations stemming from the resolution of the ocean model and the accuracy of simulating relevant physical characteristics. These factors include elements such as the position and structure of the ASF, thermocline, bathymetric resolution, and more. Further details regarding these factors are discussed in Section 4.2.

Focusing first on vertical temperature advection below ~150 m in the ASBS sector, 30N-ANN relative to the Historical simulation shows an anomalous upward temperature advection at these depths (Figure 10, top right panel—dark gray line). These depths coincide with the largest temperature increases shown in a cross-shelf

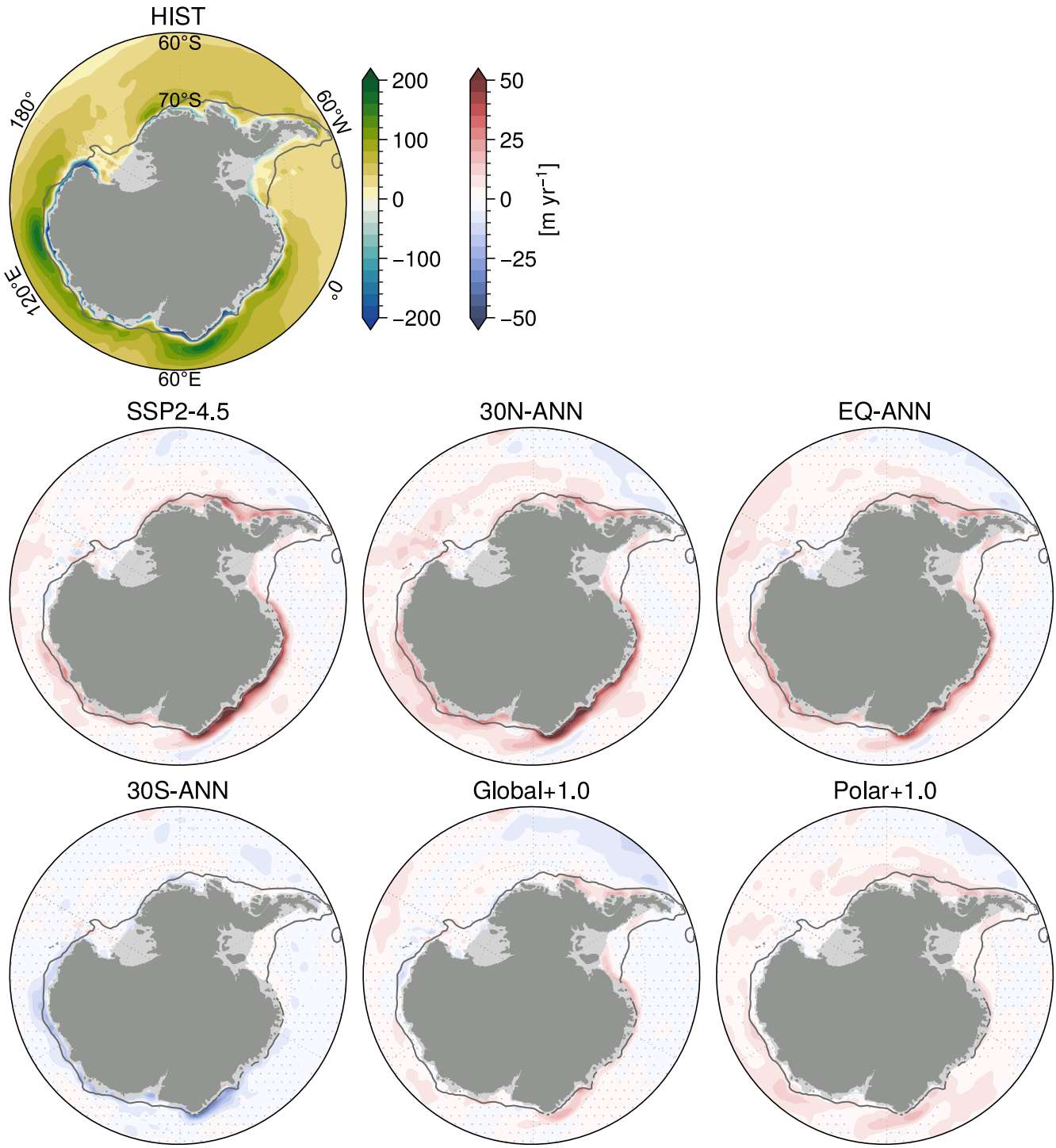

Figure 8. The top left panel shows the Historical annual ensemble mean (1990–2009) Ekman upwelling (positive values) and Ekman pumping (negative values) (m yr^{-1}). Shading in the following rows show the annual ensemble mean anomalies (2050–2069) from the Historical with respect to SSP2-4.5 and the stratospheric aerosol injection cases. Stippling shows the regions where the difference is not statistically significant. The dark gray contour follows the 1,500 m isobath.

transect through the ASE (Figure 11). Figure 10 also shows the relative contribution to the change in vertical temperature advection ($\Delta(-w \times dT/dz)$) due to changes to the vertical velocity ($-\Delta w \times d\overline{T}/dz$), to the vertical temperature gradient ($-\overline{w} \times d\Delta T/dz$), and to the interaction between these perturbations ($-\Delta w \times d\Delta T/dz$), where the overbar denotes the Historical mean. Therefore, the second row in Figure 10 for 30N-ANN relative to the Historical shows that the anomalous upward vertical temperature advection below ~150 m is primarily driven

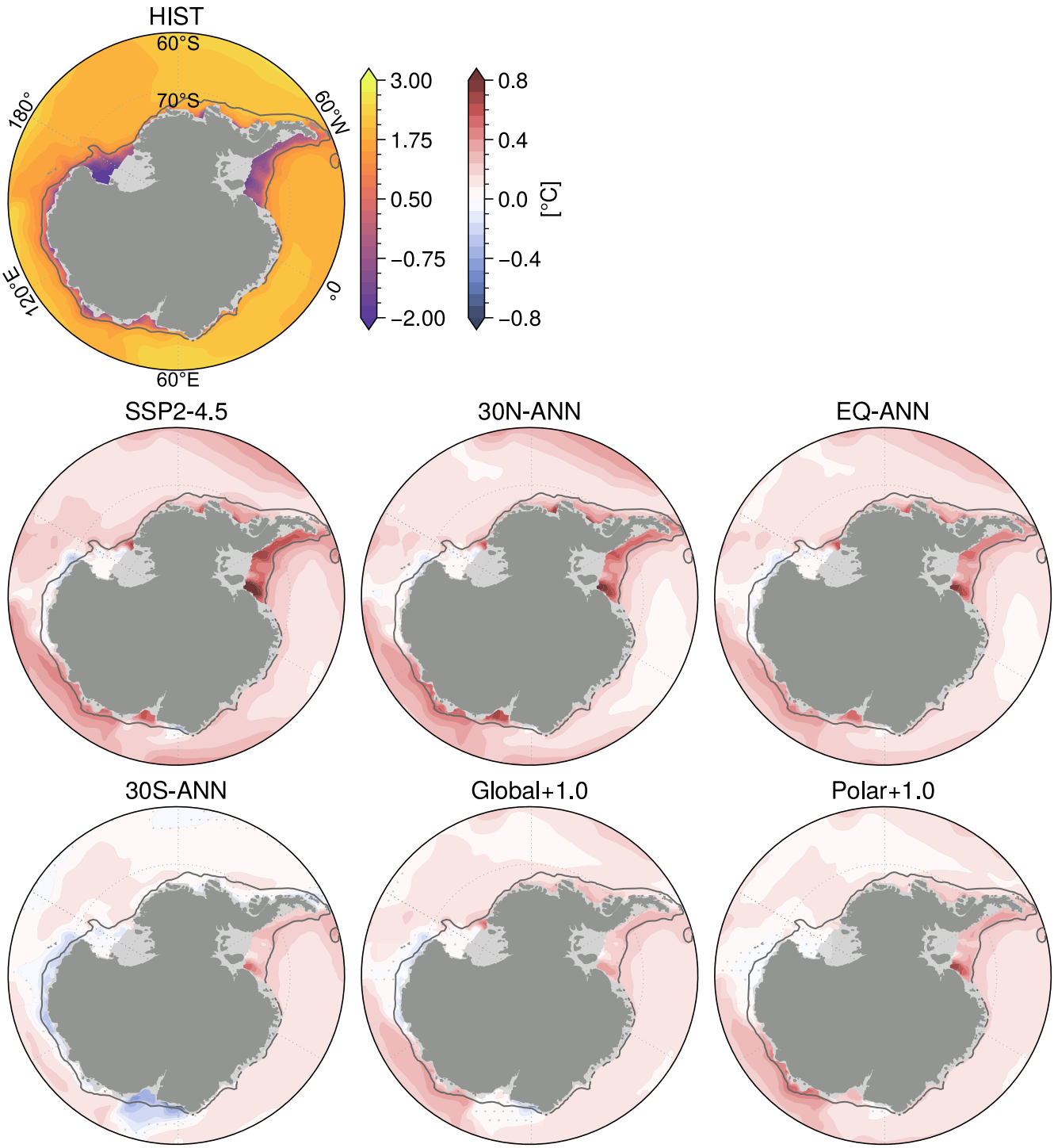

Figure 9. The top left panel shows the Historical annual ensemble mean (1990–2009) 100–1,000 m mean ocean potential temperature (°C). Shading in the following rows show the annual ensemble mean anomalies (2050–2069) from the Historical with respect to SSP2-4.5 and the stratospheric aerosol injection cases. Stippling shows the regions where the difference is not statistically significant. The dark gray contour follows the 1,500 m isobath.

by the combination of the decrease in downward vertical velocity and a decrease in the temperature gradient (a reduction in the temperature increase as depth increases—which represents a shoaling of the isotherms at these depths). These results are similar for the EQ-ANN anomalies (gray line) and the 15N-ANN anomalies (Figures S9 and S10 in Supporting Information S1).

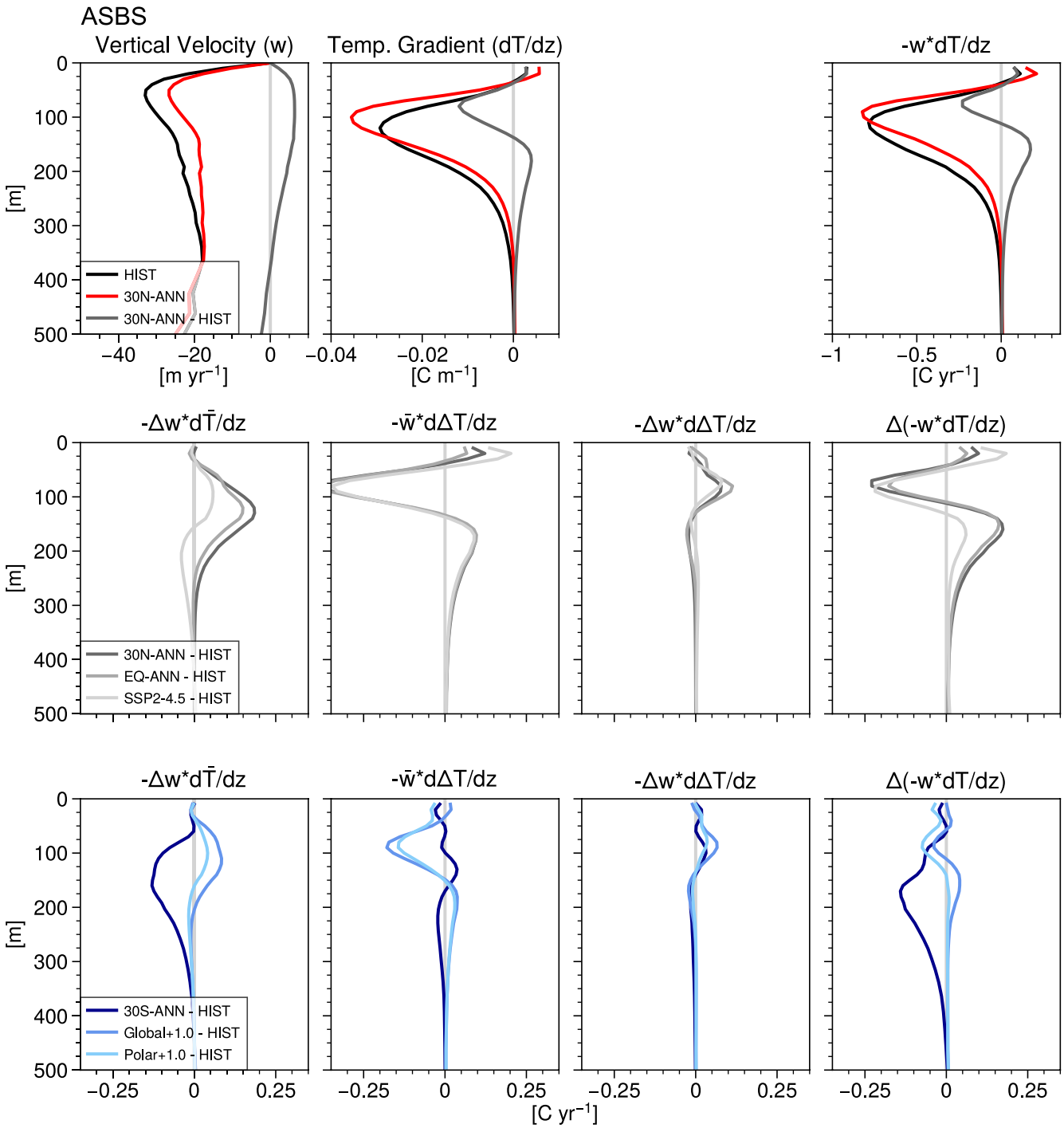

Figure 10. Vertical temperature advection and contributions to its change above the shelf in the ASBS sector. The top row shows Historical and 30N-ANN vertical velocity (m yr^{-1}), vertical temperature gradient (where negative values represent increasing temperature with increasing depth, °C m^{-1}), and vertical temperature advection (where the negative values represent a downward advection of colder surface water, °C yr^{-1}). The second and third row show the change in vertical temperature advection (far right column, $\Delta(-w \times dT/dz)$) and the contributions to this term due to the change in vertical velocity ($-\Delta w \times d\overline{T}/dz$), in the vertical temperature gradient ($-\overline{w} \times d\Delta T/dz$), and in the interaction between these perturbations ($-\Delta w \times d\Delta T/dz$), where the overbar denotes the Historical mean.

Furthermore, the upward temperature advection anomalies from below ~150 m for the 30N-ANN and EQ-ANN SAI cases are greater than for SSP2-4.5 (Figure 10, light gray line—middle row). In SSP2-4.5, the contribution of anomalous upward velocity to anomalous upward temperature advection below ~150 m is of the opposite sign compared to 30N-ANN and EQ-ANN (middle row—first panel). This strengthening of the downward vertical

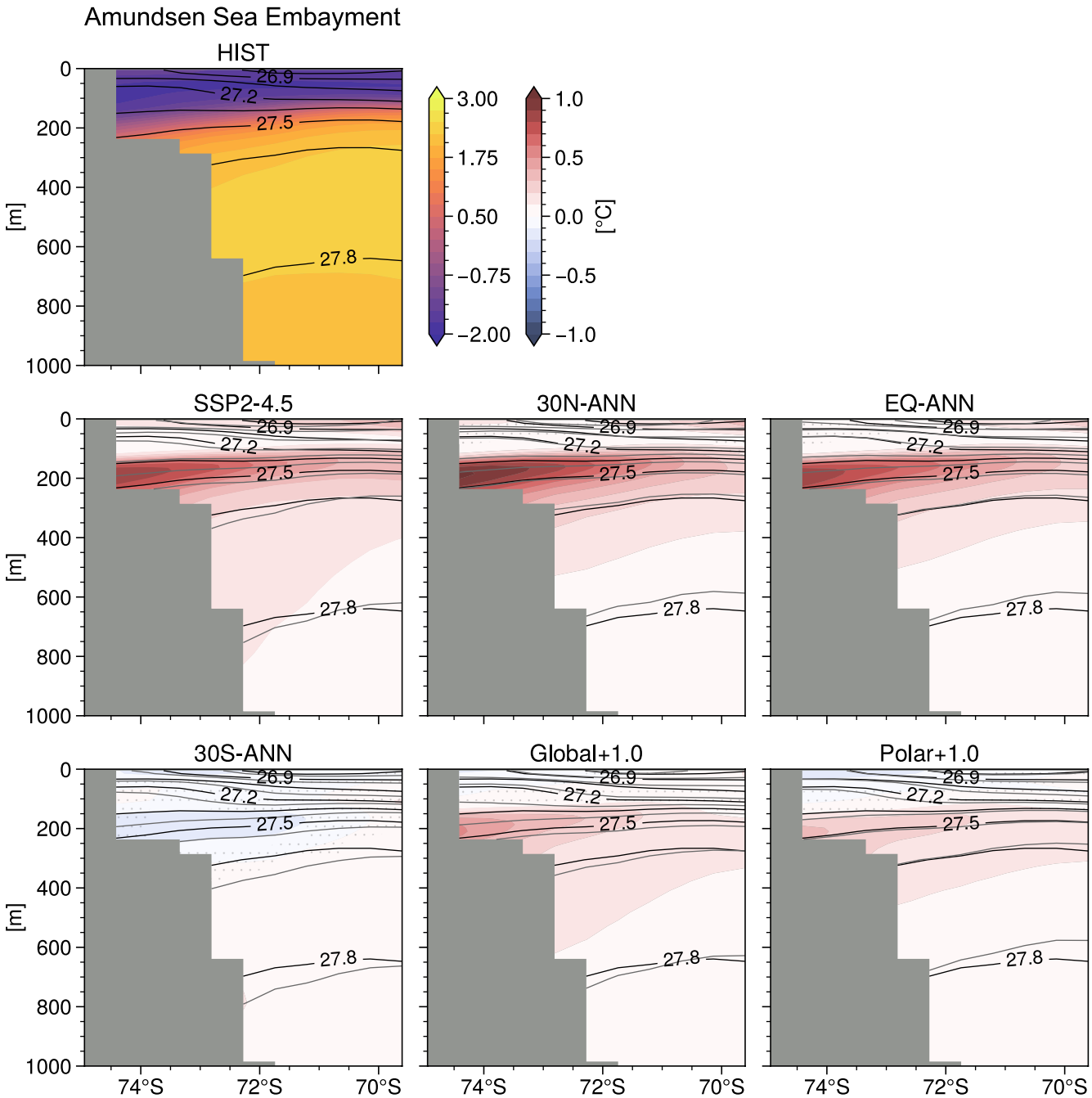

Figure 11. The top left panel shows the Amundsen Sea embayment cross-shelf transect at 106°W of potential temperature referenced to the surface (°C) with contours of constant potential density (isopycnals, minus 1,000 kg m^{-3}) for the Historical ensemble mean (1990–2009). Shading in the following rows show the annual ensemble mean temperature anomalies (2050–2069) from the Historical with respect to SSP2-4.5 and the stratospheric aerosol injection cases where stippling shows the regions where the difference is not statistically significant. In the difference panels, black contours mark the Historical isopycnals and gray contours mark the perturbed isopycnals (the lowest perturbed isopycnal is also 27.8 kg m^{-3}).

velocity at depth in SSP2-4.5 may be explained by the greater surface freshwater flux relative to these SAI cases. The freshwater flux enhances vertical stratification and prevents upward advection of CDW. The role of freshwater forcing on 100–1,000 m mean shelf temperature will be explained further below. Nonetheless, anomalous upward temperature advection persists below ~150 m in SSP2-4.5 due to the shoaling of CDW and the isotherms.

The anomalous warming below ~150 m for Global+1.0 and Polar+1.0 shown in the cross-shelf transect through the ASE (Figure 11) is also associated with a slight shoaling of the isotherms and reduction in the downward

vertical velocity as shown in the ASBS sector (Figure 10—bottom row). However, in the EAIS sector, Polar+1.0 shows greater anomalous upward temperature advection and larger shelf ocean temperature anomalies below ~150 m than Global+1.0 (Figures 12 and 13). This is due, at least in part, to slightly larger Ekman upwelling anomalies in the EAIS sector in Polar+1.0 (Figure 8) stemming from a more pronounced expression of a positive SAM phase and the associated weakening of the coastal easterly wind stress as compared to Global+1.0 (Figure 3). Another contributing factor to the enhanced upward temperature advection in Polar+1.0 relative to Global+1.0 may be associated with the larger shelf freshening and greater stratification in Global+1.0 which minimizes upward vertical velocity anomalies at these depths.

Analyzing the vertical temperature advection in the EAIS sector provides more insight to the role of freshwater forcing on 100–1,000 m mean shelf temperature. The first panel in the middle row of Figure 12 (light gray line) shows that between ~50 and 400 m there is a suppression of the upward temperature advection due to changes in the vertical velocities leading to warming at these depths in SSP2-4.5 as compared to the Historical (Figure 13). This response is opposite to the expected increase in upward temperature advection due to the anomalous Ekman upwelling in this region (Figure 8). However, a significant surface freshwater flux driven by increases in runoff in response to the ice accumulation gain and SAT increase above the nearby land in the EAIS sector (Figures 5 and 7) greatly stratifies the shelf water column preventing upward vertical velocity anomalies at these depths. This SSP2-4.5 freshening is shown in the 0–100 m mean salinity anomaly maps (Figure 14 and Figure S11 in Supporting Information S1), in the deepening of the isopycnals above ~400 m (despite weaker Ekman downwelling), and in the salinity anomalies in the cross-shelf transect in PB near the Amery Ice Shelf (Figure 15 and Figure S12 in Supporting Information S1). This stratification is shown to restrict the positive temperature anomalies to depths below ~200 m in the PB cross-shelf transect (Figure 13 and Figure S13 in Supporting Information S1).

In comparison to SSP2-4.5, both 30N-ANN and EQ-ANN show limited changes to the freshwater flux and isopycnal depth above about ~400 m within the EAIS sector permitting upward temperature advection anomalies driven by increase vertical velocity. This result is illustrated by the positive values in Figure 12 (middle row—left column). Therefore, in the Antarctic shelf ocean, our simulations show that the vertical temperature advection anomalies due to the changes to the vertical velocity term are a function of both changes to surface wind stress and surface freshwater forcing. This conclusion is supported by previous research using climate models which detail the relative contributions of freshwater forcing and wind stress changes to shelf ocean warming (e.g., Beadling et al., 2022; Bronselaer et al., 2018; Goddard et al., 2017). Finally, a cross-shelf transect of ocean salinity in the ASE is shown in Figure 16 and Figure S14 in Supporting Information S1 to aid with the analysis of the vertical temperature advection in Figure 10 and Figure S9 in Supporting Information S1, and Figure S15 in Supporting Information S1 shows vertical temperature advection in the EAIS sector for the SAI cases not included in main Figure 12.

In summary, our simulations show that Antarctic shelf ocean warming below 100 m is initiated by changes to the surface wind stress and transferred to the ocean via Ekman upwelling anomalies. For the Equator and the NH single-latitude SAI cases, these Ekman upwelling anomalies bring warm CDW onto the continental shelf and increase shelf temperatures at depths pertinent to ice shelf basal melt. Conversely, the SH single-latitude SAI cases enhance Ekman downwelling, slow onshore CDW transport, and decrease 100–1,000 m shelf temperature relative to the Historical. Both Global+1.0 and Polar+1.0 show less subsurface warming than SSP2-4.5 but vary between each other (particularly in the shelf ocean near the EAIS) due to regional differences in surface wind stress and freshwater flux anomalies. Finally, in agreement with previous studies, results shown here suggest that upward temperature advection may be limited by enhanced ocean stratification due to surface freshening.

4. Discussion

McKay et al. (2022) synthesize a multitude of studies to quantify the vulnerability of the Antarctic Ice Sheet and other climate tipping points with respect to future greenhouse gas warming. The authors estimate through their synthesis of previous work (e.g., Arthern & Williams, 2017; Feldmann & Levermann, 2015; Garbe et al., 2020; H. Yu et al., 2019) that the global mean surface temperature threshold pertaining to the eventual collapse of the WAIS is 1.5°C (min. 1.0°, max. 3.0°C) above the pre-industrial time period. Of course, this is an oversimplification and the associated uncertainty in this value is large. Each West Antarctic glacier susceptible to marine ice sheet instability will have its own unique tipping point contingent upon local ocean heat transport, ice dynamics at the groundling line, and bathymetry. Similarly, McKay et al. (2022) generate an estimate based on previous

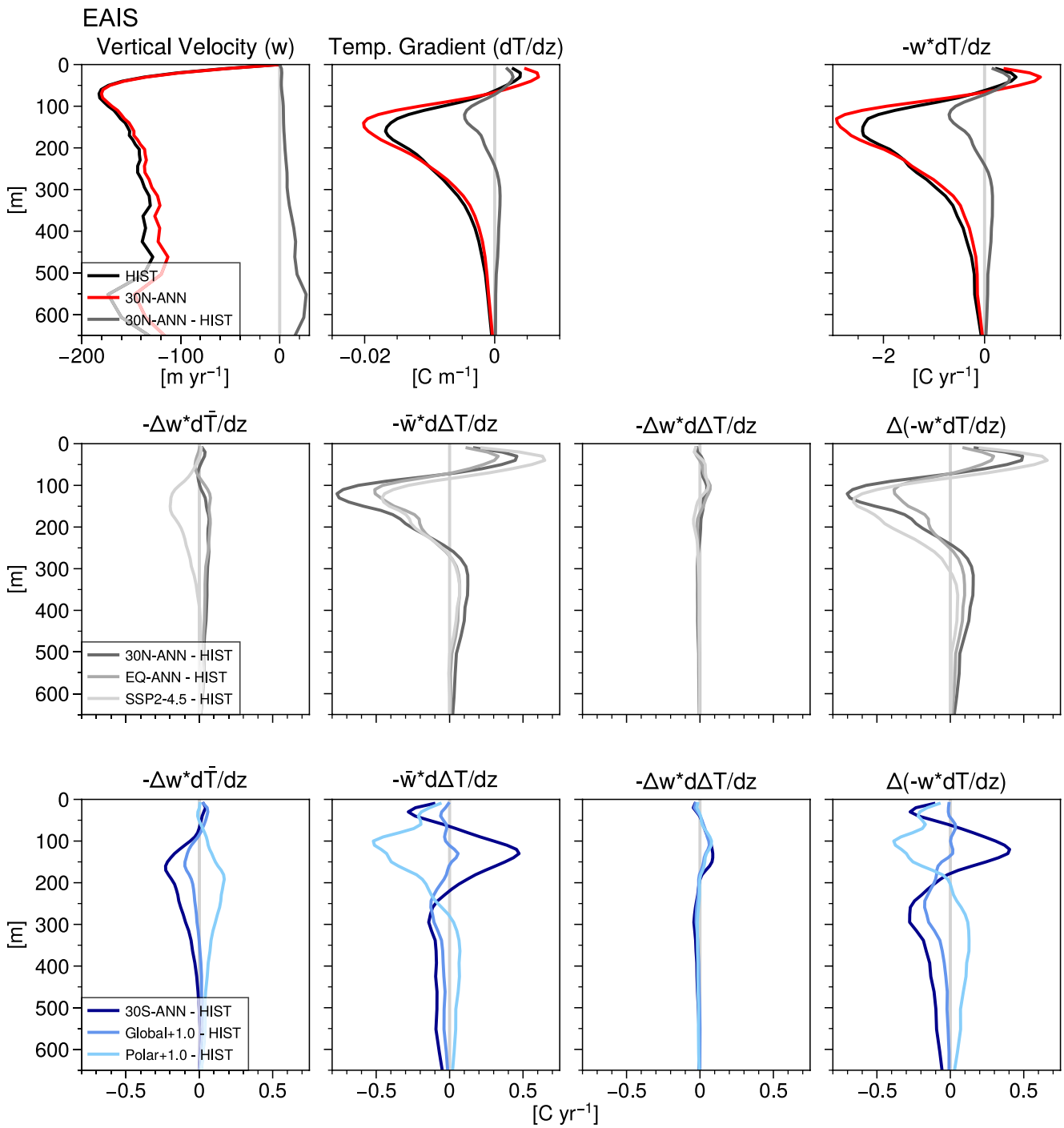

Figure 12. Same caption as for Figure 10 but showing the East Antarctic Ice Sheet sector.

work (e.g., Clark et al., 2020; DeConto et al., 2021; Edwards, 2019; Garbe et al., 2020) for a 3.0°C (min. 2.0°, max. 6.0°C) temperature threshold that is applicable to the eventual collapse of multiple subglacial basins in East Antarctica which also rest upon retrograde bedrock.

Following the SSP2-4.5 emissions pathway entails that GMT will reach the 1.5°C threshold in the early 2030s (Diffenbaugh & Barnes, 2023) and that temperatures will be nearly 3.0°C above the pre-industrial by the end of the 21st century (Meinshausen et al., 2020). If temperatures are maintained at 1.5°C or 3.0°C above the pre-industrial, the global mean sea level rise contribution from Antarctica is estimated to be about 1.0 (0.6–

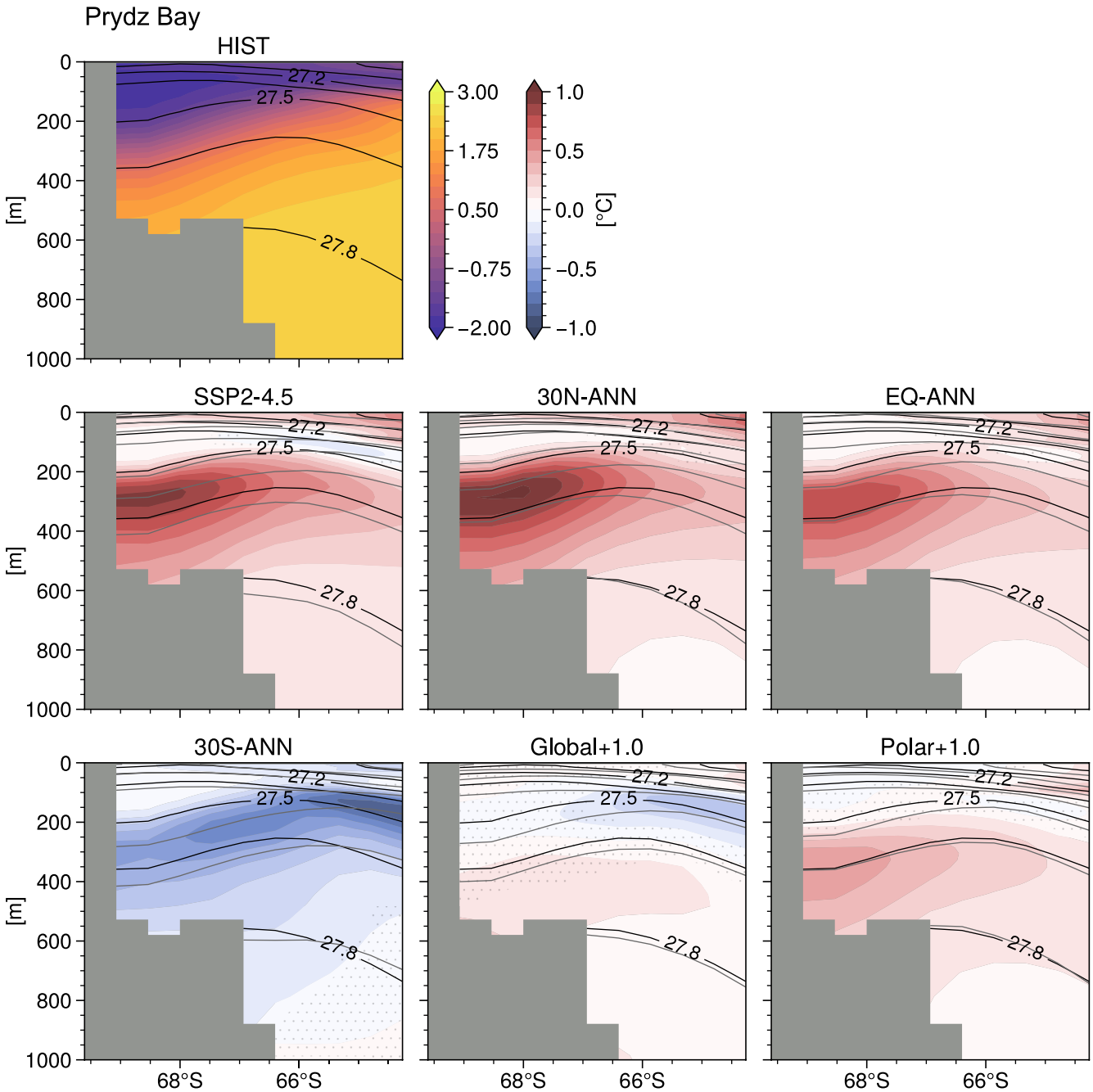

Figure 13. Same caption as for Figure 11 but showing the Prydz Bay cross-shelf transect at 74°E.

1.2) or 1.5 (1.0–2.0) meters by 2300, respectively; in comparison, the contribution is estimated to be about 9.6 (6.9–13.6, 17th-83rd percentiles) meters by 2300 if greenhouse gas emissions continue in the future along the business-as-usual RCP8.5 scenario (DeConto et al., 2021). Therefore, SAI has continued to be studied as a means of minimizing such risks and adverse impacts from exceeding these critical climate thresholds, at least until renewable energy implementation and/or carbon dioxide removal technologies are scaled globally.

4.1. Multi-Latitude SAI Cases Compared to the 21st Century SSP2-4.5 Pathway

Relevant to the estimated Antarctic Ice Sheet climate tipping points, the discussion below details whether the four multi-latitude SAI cases (Global+1.5, Global+1.0, Global+0.5, and Polar+1.0) will slow future 21st century

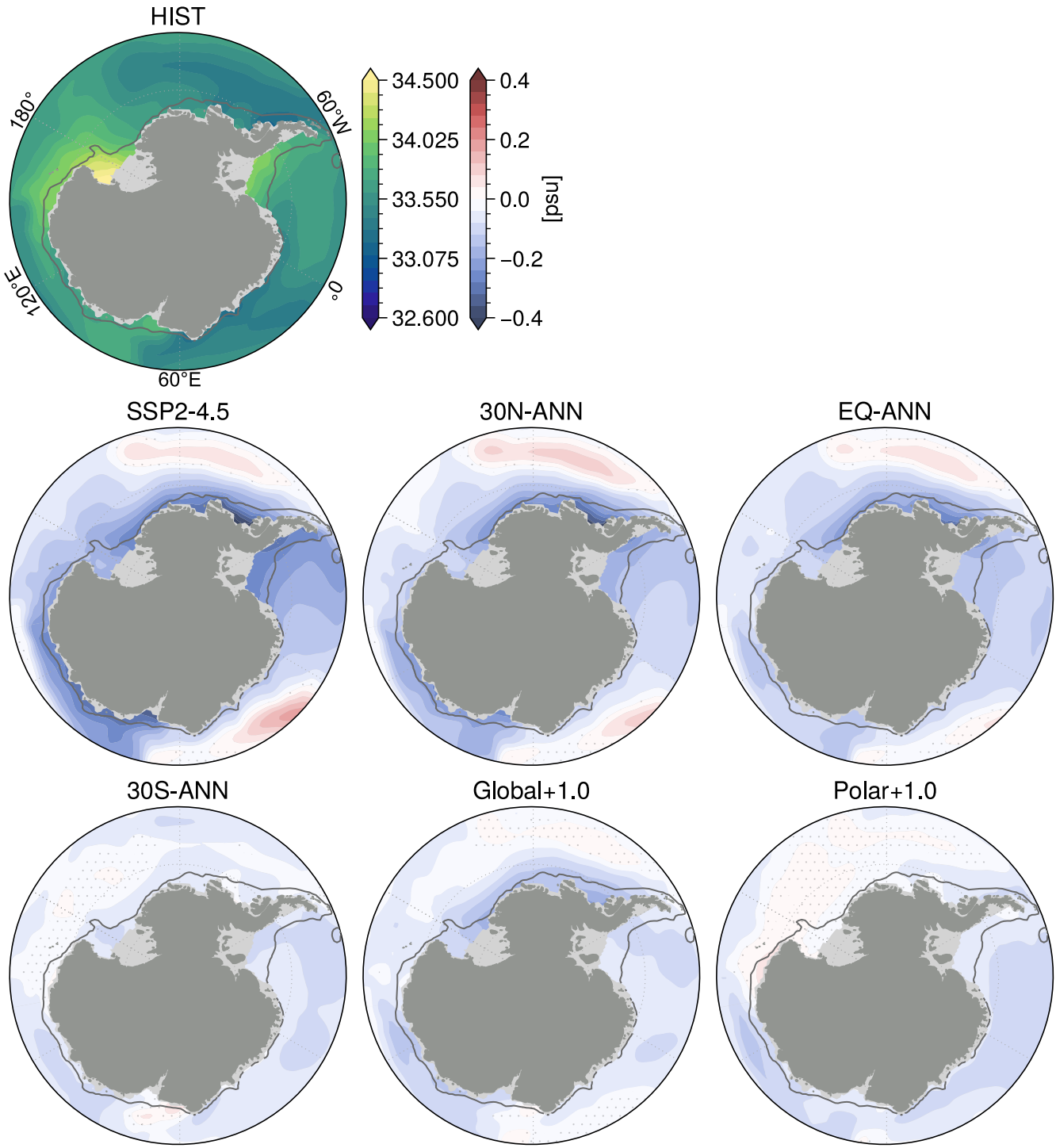

Figure 14. The top left panel shows the Historical annual ensemble mean (1990–2009) 0–100 m mean salinity (psu). Shading in the following rows show the annual ensemble mean anomalies (2050–2069) from the Historical with respect to SSP2-4.5 and the stratospheric aerosol injection cases. Stippling shows the regions where the difference is not statistically significant. The dark gray contour follows the 1,500 m isobath.

Antarctic ice loss relative to years 2020–2039 and/or 2050–2069 in the SSP2-4.5 simulation when GMT is 1.5°C and 2.4°C above the pre-industrial level, respectively. We qualitatively determine whether ice loss is slowed by evaluating changes to surface ice accumulation and subsurface shelf ocean temperatures. However, we note that coupled ice sheet simulations would be necessary to quantify the relative change in ice mass.

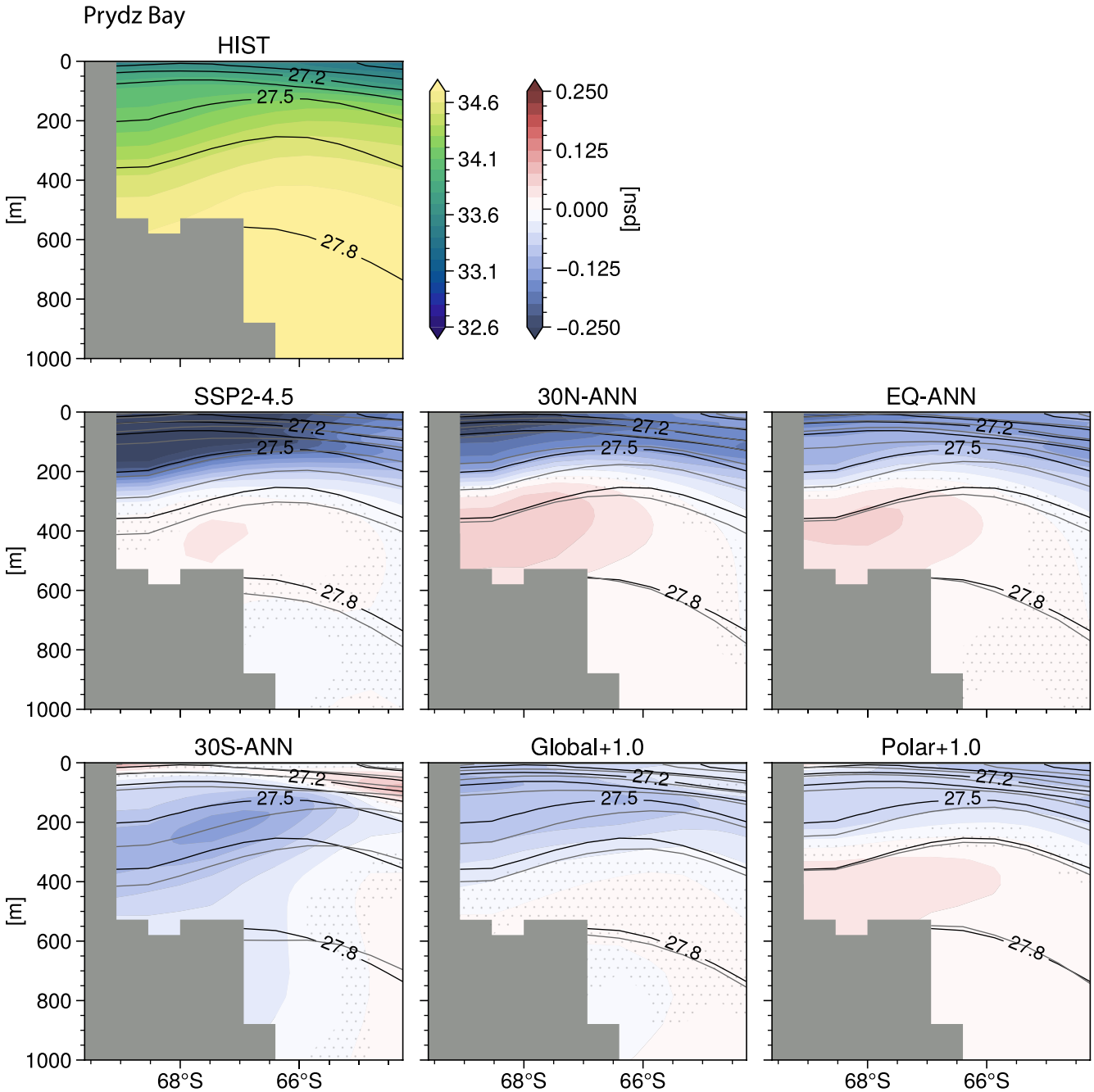

Figure 15. The top left panel shows the Prydz Bay cross-shelf transect at 74°E of salinity (psu) with contours of constant potential density (isopycnals, minus 1,000 kg m^{-3}) for the Historical ensemble mean (1990–2009). Shading in the following rows show the annual ensemble mean temperature anomalies (2050–2069) from the Historical with respect to SSP2-4.5 and the stratospheric aerosol injection cases where stippling shows the regions where the difference is not statistically significant. In the difference panels, black contours mark the Historical isopycnals and gray contours mark the perturbed isopycnals (the lowest perturbed isopycnal is also 27.8 kg m^{-3}).

For this assessment, Figure 17 shows the annual ensemble mean area integrated ice accumulation (middle row) and the 100–1000 m mean shelf ocean temperature (bottom row) with respect to the Historical time period (1990–2009) for the WAIS, EAIS, or entire continent (columns) for each of the multi-latitude SAI cases, SSP2-4.5 (2020–2039), and SSP2-4.5 (2050–2069) relative to the GMT change from the pre-industrial for each ensemble mean (independent axis). This figure illustrates whether these SAI cases overcompensate (yellow shaded region) or undercompensate (green shaded region) these scalar metrics relative to the GMT change from the

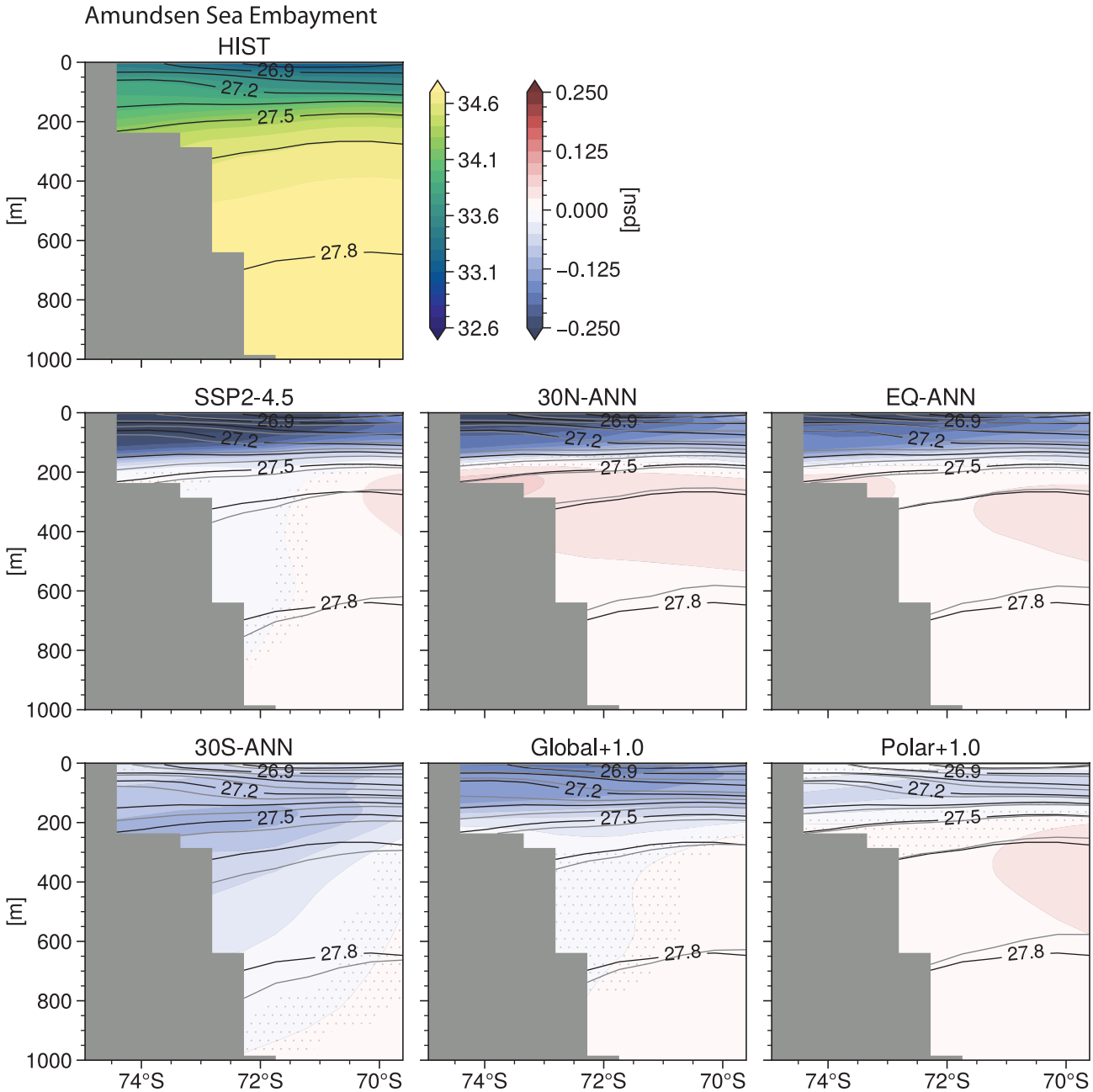

Figure 16. Same caption as for Figure 15 but showing the Amundsen Sea embayment cross-shelf transect at 106°W.

Historical-to-SSP2-4.5 pathway. The spatial response of the ice accumulation and subsurface shelf ocean temperature for these SAI cases with respect to SSP2-4.5 (2020–2039) and SSP2-4.5 (2050–2069) are shown in Figures S16 and S17 of Supporting Information S1.

Figure 17 also shows in top left panel (a) the SLP difference between 40° and 65°S which represents the strength of the SAM (Gong & Wang, 1999; Marshall, 2003) relative to the GMT change for each of the simulation ensembles. Along the Historical-to-SSP2-4.5 pathway the SLP difference increases with increasing GMT—this highlights the projected 21st century positive SAM trend (Coburn & Pryor, 2022; Zheng et al., 2013). This panel also illustrates that Polar+1.0 will result in a more robust positive SAM pattern than is projected along the Historical-to-SSP2-4.5 pathway; and shows that for all the Global+ cases the SLP difference represents a negative SAM pattern relative to the Historical-to-SSP2-4.5 pathway. This relative overcompensation in Polar+1.0

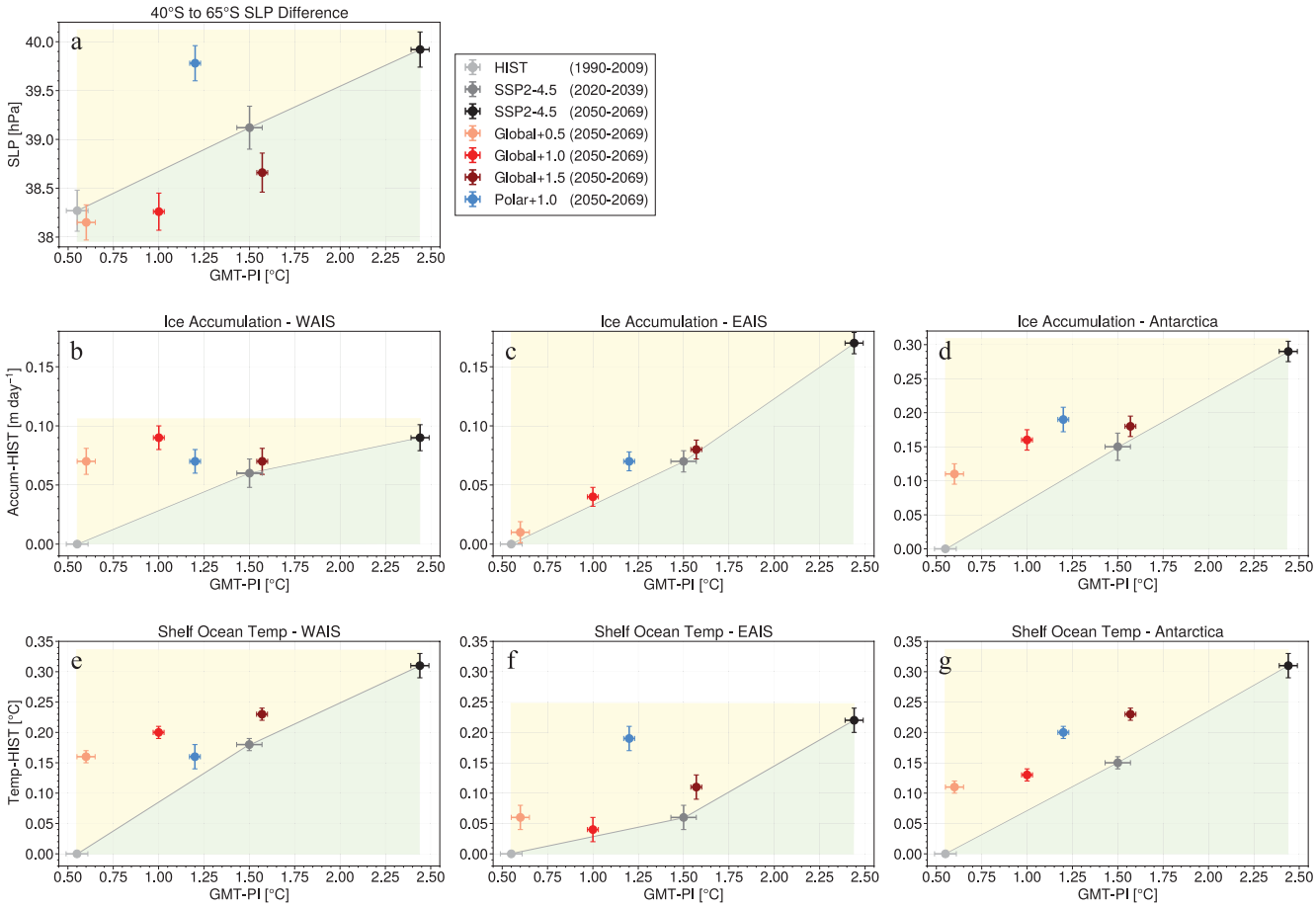

Figure 17. Scalar metrics versus the global mean temperature change from the pre-industrial (independent axis) for the Historical, SSP2-4.5, and multi-latitude stratospheric aerosol injection (SAI) cases. The top-left panel (a) shows the zonal mean sea level pressure difference from 40° to 65°S. The middle row shows the integrated surface ice accumulation (m day^{-1}, with respect to the Historical) across the West Antarctic Ice Sheet (WAIS) (from about 145° to 80°W), East Antarctic Ice Sheet (EAIS) (from about 15°W to 163°E), and the whole continent. The bottom row shows 100–1000 m mean shelf ocean temperature (°C, with respect to the Historical) across the WAIS, EAIS, and whole continental shelf. All values represent the ensemble mean for years listed in the legend. The yellow and green shaded regions represent an overcompensation or undercompensation by the SAI case relative to the Historical-to-SSP2-4.5 pathway (the gray line segments connecting the Historical, SSP2-4.5 (2020–2039), and SSP2-4.5 (2050–2069) circles). The error bars represent plus-minus 1 standard error.

and undercompensation in the Global+ cases is consistent with the SLP and surface wind stress anomaly patterns shown in Figure 3 and Figure S2 in Supporting Information S1 and critically influences ice accumulation and shelf ocean temperature patterns as examined in the Results section.

Regarding simulated mass changes to the WAIS, Figure 17b shows that there is an overcompensation of ice accumulation per unit increase in GMT in the multi-latitude SAI cases relative to the Historical-to-SSP2-4.5 pathway. Notably, for each of these SAI cases WAIS snow accumulation will be greater than the SSP2-4.5 2020–2039 mean accumulation. This increase signifies that all of the multi-latitude SAI cases will accumulate more WAIS ice at the surface through precipitation as compared to the SSP2-4.5 time period when the GMT reaches 1.5°C (2020–2039). Nonetheless, this increase in ice accumulation is likely to play a secondary role in the change to the overall WAIS mass balance as previous research shows that the WAIS projected mass change will be dominated by ice shelf basal melt due to ocean thermal forcing (Chambers et al., 2022; Siahaan et al., 2022).

Figure 17e shows that there would be an overcompensation of the mean subsurface shelf ocean temperature near the WAIS in these multi-latitude SAI cases, indicating that the regional ocean is warmer per unit increase in GMT than along the Historical-to-SSP2-4.5 pathway. Markedly, the Global+1.5 (dark red circle) and Global+1.0 (red circle) cases result in warmer shelf ocean temperatures near the WAIS as compared to SSP2-4.5 (2020–2039) when the GMT is 1.5°C above the pre-industrial (gray circle). Of the multi-latitude injection cases considered in this study only the Polar+1.0 and Global+0.5 cases keep WAIS shelf ocean temperatures below SSP2-4.5

(2020–2039) which represents an estimated climate tipping point temperature threshold for the self-perpetuating, eventual collapse of the WAIS as synthesized in McKay et al. (2022). Therefore, to hold shelf ocean temperatures near the WAIS below this threshold through the mid-to-late 21st century (2050–2069), our simulations suggest that SAI would have to cool GMT by 1.0°C if considering a multi-latitude injection at low latitudes (i.e., Global+0.5) or by 0.5°C if considering a high-latitude injection case (i.e., Polar+1.0). That said, it is important to note that all multi-latitude SAI cases considered here simulate shelf ocean temperatures near the WAIS that are significantly below the mean value of SSP2-4.5 during 2050–2069 (black circle).

Regarding the EAIS, previous observations show the presence of CDW (or modified CDW) on the shelf and increased basal melt rates at locations between PB and the Ross Sea (Figure 1) (e.g., Greenbaum et al., 2015; Rignot et al., 2019; B. Smith et al., 2020). This area includes two subglacial basins near the George V Land and Wilkes Land that are vulnerable to rapid melting if the warm CDW reaches the regional ice shelves (Herraiz-Borreguero & Naveira Garabato, 2022; Iizuka et al., 2023). Through their research synthesis, McKay et al. (2022) estimate that for these East Antarctic subglacial basins to become high risk for collapse the GMT above the pre-industrial threshold is ∼3.0°C, with a minimum threshold of 2.0°. Therefore, to minimize the risk of these subglacial basins, we now discuss each multi-latitude SAI case relative to the SSP2-4.5 pathway when GMT is at least 2.0°C above the pre-industrial.

Figure 17f shows the mean subsurface shelf ocean temperature change near the EAIS (relative to the Historical) per unit increase in GMT for the multi-latitude SAI cases and the Historical-to-SSP2-4.5 pathway. Although the three Global+ cases warm the regional shelf ocean more than the Historical-to-SSP2-4.5 pathway (an overcompensation), all temperatures are significantly lower than the mean shelf temperature increase (∼0.15°C) associated with a +2.0°C GMT increase and the low-end temperature threshold for the EAIS subglacial basins climate tipping point as proposed by McKay et al. (2022). Conversely, the EAIS shelf warming in the Polar+1.0 strategy (blue circle) is greater than the low-end temperature threshold and is not statistically different from the SSP2-4.5 2050–2069 mean (black circle) wherein GMT is about 2.4°C above the pre-industrial. This simulated EAIS shelf warming result in Polar+1.0 is driven by the positive SAM response, weakening coastal easterlies, and increased CDW upwelling shown in the Results section. Furthermore, the Polar+1.0 surface ice accumulation overcompensation (Figure 17c) is far less than the shelf ocean warming overcompensation which implies that the EAIS mass loss under the Polar+1.0 case would be more similar to the mid-to-late century SSP2-4.5 pathway than a pathway that uses a Global+ injection strategy.

Integrating these results across all of Antarctica, we highlight here that our simulations suggest that the Global+0.5 or Global+1.0 SAI cases demonstrate distinct benefits concerning ice mass balance as compared to the Global+1.5 or Polar+1.0 cases as well as to the SSP2-4.5 pathway with no SAI. Figure 17d shows that relative to the Historical-to-SSP2-4.5 pathway, Global+0.5 and Global+1.0 overcompensate Antarctic surface ice accumulation as much or more than the Global+1.5 or Polar+1.0 SAI cases relative to the Historical-to-SSP2-4.5 pathway. Therefore, the simulated atmospheric circulation changes induced by Global+0.5 and Global+1.0 (namely the onshore winds near the WAIS due to the developed Pacific-South America pattern, Figure 3 and Figure S2 in Supporting Information S1) bring more snow and ice accumulation to the Antarctic continent relative to the change in GMT and relative to Global+1.5 or Polar+1.0 (as well as the Historical-to-SSP2-4.5 pathway). Furthermore, in both Polar+1.0 and Global+1.5 the mean Antarctic shelf ocean temperature is significantly warmer due to associated changes in CDW upwelling as compared to Global+0.5 and Global+1.0. Finally, despite similar integrated ice accumulation and mean shelf ocean temperature across Antarctica, it is important to recall that Global+0.5 keeps the WAIS shelf ocean temperature below that associated with the estimated 1.5°C temperature threshold, while Global+1.0 exceeds this threshold and thus incurs a greater risk of driving a WAIS collapse. Therefore, for our simulations utilizing SAI to cool GMT to 0.5°C above the pre-industrial, as represented by the Global+0.5 case, would be needed to minimize these risks to the Antarctic Ice Sheet.

Our findings emphasize the importance of clearly defining both the cooling objectives and injection locations when discussing the potential of SAI to mitigate the impacts of greenhouse warming on the Antarctic ice sheets. For instance, Sutter et al. (2023) mainly highlight SAI cases that cannot prevent WAIS collapse. Most of their SAI cases deploy after GMT is already above 1.5°C above pre-industrial, and they do not consider cooling below the temperature at the start of deployment. Furthermore, all of their cases inject more in the NH than the SH and include a significant injection portion near the Equator. The results presented from our simulations show that the latitudinal dispersion of aerosols in Sutter et al. (2023) would lead to greater warming of the shelf waters

than injection cases that have a greater concentration in the SH between about 15° and 30°S. The only SAI cases presented in Sutter et al. (2023) that may prevent WAIS collapse is where SAI is started in or before the year 2040 and GMT is kept to about 1.5°C above pre-industrial. The authors note that the 2040 case still carries a substantial risk as 35% of their models show that WAIS will still collapse. Therefore, it is important to note that the Sutter et al. (2023) conclusions are specific to their chosen SAI strategy (the latitudinal dispersion and the target value for GMT) and differ from the more generalizable result presented in our Figure 17. According to our simulations, the effectiveness of SAI to minimize the risk of a WAIS collapse depends on the chosen cooling amount and the latitudinal injection dispersion. As noted previously, to minimize risk of a WAIS collapse, our simulations suggest that SAI would need to be deployed early, reduce GMT below the temperature at the start of deployment (e.g., to 0.5°C above the pre-industrial), and inject at latitudes between 30°S and 30°N with a greater proportion injected in the SH. Moving forward, this consideration should inform the evaluation of trade-offs between higher and lower amounts of SAI.

4.2. Limitations and Future Work

While the high-latitude SH atmospheric response to various SAI cases shown in this study is consistent with previous SAI studies (Bednarz et al., 2022; McCusker et al., 2015), the role SAI can play in the Antarctic region has generally not yet been extensively studied and as such remains relatively poorly understood. The detailed evaluation of the Antarctic shelf ocean response to multiple SAI cases (which latitude(s) and amount of cooling) has not, to our knowledge, been performed before and as such our work constitutes a novel contribution to this research field for which direct comparisons to previous SAI research are minimal. It is therefore important to discuss the relevant limitations of the model and concerns regarding its representation of the shelf ocean physics. One key limitation is the relatively weak lateral density gradient associated with the ASF in these simulations as compared to observations (e.g., the World Ocean Circulation Experiment, Sparrow et al. (2011)) and other studies which examine cross-ASF heat transport using higher resolved ocean models (e.g., Goddard et al., 2017; Palóczy et al., 2018; Stewart et al., 2018). The weak ASF is characterized by flatter isopycnals near the shelf break (see contours in Figures 11 and 13) which create additional pathways for along-isopycnal onshore transport of CDW as compared to these previous studies and observations. Conversely, the horizontal ocean resolution in the current study (~1° at 70°S) is too coarse to resolve ocean eddies which are an important mechanism for onshore heat transport through the ASF (e.g., Goddard et al., 2017; Palóczy et al., 2018; Stewart et al., 2018).

Furthermore, previous studies show that the model representation of the ASF is critical to the effect that surface freshwater forcing has on CDW-induced shelf warming. Namely, in models with <0.25° horizontal resolution the shelf ocean surface freshening promotes a strengthening of the ASF which keeps the freshwater on the shelf, strengthens the ASF, and minimizes onshore cross-ASF heat transport (Beadling et al., 2022; Goddard et al., 2017; Moorman et al., 2020). Conversely, in coarser ocean models the surface freshening anomalies can extend away from the continental shelf and stratify the surface layers which flatten the isopycnals that would otherwise reach the surface and transport heat to the overlying atmosphere or sea ice. Instead, the heat is directed toward the shelf along the flattened isopycnals (Beadling et al., 2022; Bronselaer et al., 2018; Golledge et al., 2019). In the current study, the interaction between the ASF, surface freshening, and shelf warming are more aligned with the second set of studies wherein a relatively weak ASF permits onshore heat transport at depth along relatively flat isopycnals. This heat is then maintained above the continental shelf due to surface freshening and the resultant vertical stratification which reduces upward vertical heat advection (see Figures 10–13). The relative role of increased melt flux into the shelf ocean and its effect on shelf temperatures remains an active area of research in the ocean modeling community.

Despite uncertainties regarding the impact of freshwater forcing and numerical limitations of the ocean model used in this study, the subsurface shelf ocean temperature response in SSP2-4.5 are consistent with previous studies which show a similar temperature response with respect to changes to the coastal easterlies (e.g., Beadling et al., 2022; Goddard et al., 2017; Spence et al., 2014). Additionally, the results here are consistent with Palóczy et al. (2018) that shows shelf ocean warming during a positive phase SAM (weaker coastal easterlies) along the WAIS coastline and western Antarctic Peninsula coastline as well as in the eastern-EAIS region.

Moving forward, it would be beneficial to have a coupled Antarctic ice sheet to facilitate a quantitative mass balance analysis (e.g., Sutter et al., 2023). This addition would improve the current assessment of Antarctic ice loss, which qualitatively assesses whether ice loss would decrease in the multi-latitude SAI cases by looking at

relative changes to ice accumulation and shelf ocean temperature as compared to SSP2-4.5. Furthermore, Fasullo and Richter (2023) show that rapid climate adjustments to CO_2 forcing can vary significantly from model to model and thus the choice of the background emission scenario in an SAI simulation is vital to the simulated output. Therefore, a quantitative assessment of the impacts of varying SAI strategies on the Antarctic ice mass balance should be performed in a multi-model framework in order to narrow the uncertainty arising from model representation of various physical processes. Additionally, in this study the Global+ cases injected the majority of the SO_4 precursors in the southern hemisphere which led to atmospheric circulation changes more beneficial to Antarctic ice than the response if the major of the injection was in the northern hemisphere. Future work will build upon the Global+ SAI cases to see whether changes to the injection strategy, in a manner introduced in Zhang et al. (2023) and Bednarz et al. (2023), would further slow Antarctic mass loss.

5. Conclusions

This study uses seven different single-latitude SAI cases and four different multi-latitude SAI cases to assess the resulting SAI impacts on the Antarctic climate, namely surface ice accumulation and subsurface shelf ocean temperature. These cases are compared to a historical time period (1990–2009) and to select time periods along the 21st century SSP2-4.5 emissions pathway that represent estimated GMT thresholds relevant to Antarctic ice sheet tipping points. Of the multi-latitude SAI cases, we find that the Global+0.5 or the Polar+1.0 case can maintain subsurface shelf ocean temperatures near the WAIS below the temperature threshold that is estimated to initiate the eventual collapse of the ice sheet, though the uncertainty in this number is large (McKay et al., 2022). However, relative to three Global+(0.5, 1.0, 1.5) cases, the Polar+1.0 strategy significantly warms the shelf ocean near the East Antarctic Ice Sheet (EAIS) and results in ocean temperatures above the low-end estimate for the tipping point of subglacial basins in the EAIS (McKay et al., 2022). This is due to the Polar+1.0 case simulating southern hemisphere SLP and wind stress anomalies with respect to the Historical simulation analogous to patterns correlated with the positive phase of the SAM. Around East Antarctica in particular, this positive mode is associated with weaker coastal easterlies and more upwelling of warm CDW onto the continental shelf at depths pertinent to ice shelf basal melt. Therefore, for the multi-latitude SAI cases considered here, the Global+0.5 SAI strategy would minimize the most risk associated with the future melt and potential collapse of significant regions of the Antarctic Ice Sheet.

In summary, while some of the results could be model dependent, our CESM2(WACCM6) simulations demonstrate that the multi-latitude SAI cases considered here all slow Antarctic ice loss relative to the mid-to-late century SSP2-4.5 pathway, though using SAI to cool global mean temperatures to 0.5°C above the pre-industrial (the Global+0.5 case) may be necessary to avoid estimated Antarctic ice sheet tipping points. These results highlight the complexity of factors driving the SAI-induced impacts on the Antarctic system and demonstrate the crucial role of the injection strategy in determining the effectiveness of SAI in preventing future losses of Antarctic ice.

Acknowledgments
This research was supported in part by Lilly Endowment, Inc., through its support for the Indiana University Pervasive Technology Institute. Support for BK was provided in part by the National Science Foundation through agreement SES-1754740, NOAA's Climate Program Office, Earth's Radiation Budget (Grant NA22OAR4310479), and the Indiana University Environmental Resilience Institute. The Pacific Northwest National Laboratory is operated for the US Department of Energy by Battelle Memorial Institute under contract DE-AC05-76RL01830. We would like to acknowledge high-performance computing support from Cheyenne (https://doi.org/10.5065/D6RX99HX) provided by NCAR's Computational and Information Systems Laboratory, sponsored by the National Science Foundation. Support was also provided by the Atkinson Center for Sustainability at Cornell University, and by the National Science Foundation through agreement CBET-2038246. EMB also acknowledges support from the NOAA cooperative agreement NA22OAR4320151 and the NOAA Earth's Radiative Budget initiative.

Data Availability Statement

The simulation data for the Historical, SSP2-4.5, and Global+1.0 and the analysis code (.ipynb/Jupyter notebooks) are available for download from zenodo.org (Goddard, 2023a, 2023b, 2023c, 2023d, 2023e). Due to dataset size limits, these data are separated into five different datasets with titles of "Data and Code for Goddard et al., 2023—SAI and Antarctica (1–5)." For other SAI simulations, please contact the corresponding author.

References

Adusumilli, S. A., Fish, M., Fricker, H. A., & Medley, B. (2021). Atmospheric river precipitation contributed to rapid increases in surface height of the West Antarctic ice sheet in 2019. *Geophysical Research Letters*, *48*(5), e2020GL091076. https://doi.org/10.1029/2020GL091076

Arthern, R. J., & Williams, C. R. (2017). The sensitivity of West Antarctica to the submarine melting feedback. *Geophysical Research Letters*, *44*(5), 2352–2359. https://doi.org/10.1002/2017GL072514

Beadling, R. L., Krasting, J. P., Griffies, S. M., Hurlin, W. J., Bronselaer, B., Russell, J. L., et al. (2022). Importance of the Antarctic Slope Current in the Southern Ocean response to ice sheet melt and wind stress change. *Journal of Geophysical Research: Oceans*, *127*(5), e2021JC017608. https://doi.org/10.1029/2021JC017608

Bednarz, E. M., Visioni, D., Kravitz, B., Jones, A., Haywood, J. M., Richter, J., et al. (2023). Climate response to off-equatorial stratospheric sulfur injections in three Earth system models – Part 2: Stratospheric and free-tropospheric response. *Atmospheric Chemistry and Physics*, *23*(1), 687–709. https://doi.org/10.5194/ACP-23-687-2023

Bednarz, E. M., Visioni, D., Richter, J. H., Butler, A. H., & MacMartin, D. G. (2022). Impact of the latitude of stratospheric aerosol injection on the Southern Annular Mode. *Geophysical Research Letters*, *49*(19), e2022GL100353. https://doi.org/10.1029/2022GL100353

Berdahl, M., Robock, A., Ji, D., Moore, J. C., Jones, A., Kravitz, B., & Watanabe, S. (2014). Arctic cryosphere response in the Geoengineering Model Intercomparison Project G3 and G4 scenarios. *Journal of Geophysical Research: Atmospheres*, *119*(3), 1308–1321. https://doi.org/10.1002/2013JD020627

Bronselaer, B., Winton, M., Griffies, S. M., Hurlin, W. J., Rodgers, K. B., Sergienko, O. V., et al. (2018). Change in future climate due to Antarctic meltwater. *Nature*, *564*(7734), 53–58. https://doi.org/10.1038/s41586-018-0712-z

Budyko, M. I. (1974). *Izmeniya Klimata. Gidrometeoizdat, also published as: Budyko, M. I. 1977 Climatic changes (transl. Izmeniia Klimata Leningrad: Gidrometeoizdat, 1974)*. American Geophysical Union.

Bull, C. Y. S., Jenkins, A., Jourdain, N. C., Vaňková, I., Holland, P. R., Mathiot, P., et al. (2021). Remote Control of Filchner-Ronne ice shelf melt rates by the Antarctic slope current. *Journal of Geophysical Research: Oceans*, *126*(2), e2020JC016550. https://doi.org/10.1029/2020JC016550

Chambers, C., Greve, R., Obase, T., Saito, F., & Abe-Ouchi, A. (2022). Mass loss of the Antarctic ice sheet until the year 3000 under a sustained late-21st-century climate. *Journal of Glaciology*, *68*(269), 605–617. https://doi.org/10.1017/JOG.2021.124

Clark, P. U., He, F., Golledge, N. R., Mitrovica, J. X., Dutton, A., Hoffman, J. S., & Dendy, S. (2020). Oceanic forcing of penultimate deglacial and last interglacial sea-level rise. *Nature*, *577*(7792), 660–664. https://doi.org/10.1038/s41586-020-1931-7

Clem, K. R., Renwick, J. A., & McGregor, J. (2017). Relationship between eastern tropical Pacific cooling and recent trends in the Southern Hemisphere zonal-mean circulation. *Climate Dynamics*, *49*(1–2), 113–129. https://doi.org/10.1007/S00382-016-3329-7/FIGURES/14

Coburn, J., & Pryor, S. C. (2022). Evolution of the internal climate modes under future warming. *Journal of Climate*, *36*(2), 511–529. https://doi.org/10.1175/JCLI-D-22-0200.1

Crutzen, P. J. (2006). Albedo enhancement by stratospheric sulfur injections: A contribution to resolve a policy dilemma? *Climate Change*, *77*(3–4), 211–220. https://doi.org/10.1007/s10584-006-9101-y

Daae, K., Hattermann, T., Darelius, E., Mueller, R. D., Naughten, K. A., Timmermann, R., & Hellmer, H. H. (2020). Necessary conditions for warm inflow toward the Filchner Ice Shelf, Weddell Sea. *Geophysical Research Letters*, *47*(22), e2020GL089237. https://doi.org/10.1029/2020GL089237

Dai, Z., Weisenstein, D. K., & Keith, D. W. (2018). Tailoring meridional and seasonal radiative forcing by sulfate aerosol solar geoengineering. *Geophysical Research Letters*, *45*(2), 1030–1039. https://doi.org/10.1002/2017GL076472

Danabasoglu, G., Bates, S. C., Briegleb, B. P., Jayne, S. R., Jochum, M., Large, W. G., et al. (2012). The CCSM4 ocean component. *Journal of Climate*, *25*(5), 1361–1389. https://doi.org/10.1175/JCLI-D-11-00091.1

Danabasoglu, G., Lamarque, J. F., Bacmeister, J., Bailey, D. A., DuVivier, A. K., Edwards, J., et al. (2020). The Community Earth System Model Version 2 (CESM2). *Journal of Advances in Modeling Earth Systems*, *12*(2), e2019MS001916. https://doi.org/10.1029/2019MS001916

Davis, N. A., Visioni, D., Garcia, R. R., Kinnison, D. E., Marsh, D. R., Mills, M. J., et al. (2022). Climate, variability, and climate sensitivity of "Middle Atmosphere" chemistry configurations of the Community Earth System Model Version 2, Whole Atmosphere Community Climate Model Version 6 (CESM2(WACCM6)). *Authorea Preprints*. https://doi.org/10.22541/ESSOAR.167117634.40175082/V1

Davison, B. J., Hogg, A. E., Rigby, R., Veldhuijsen, S., van Wessem, J. M., van den Broeke, M. R., et al. (2023). Sea level rise from West Antarctic mass loss significantly modified by large snowfall anomalies. *Nature Communications*, *14*(1), 1–13. https://doi.org/10.1038/s41467-023-36990-3

DeConto, R. M., & Pollard, D. (2016). Contribution of Antarctica to past and future sea-level rise. *Nature*, *531*(7596), 591–597. https://doi.org/10.1038/nature17145

DeConto, R. M., Pollard, D., Alley, R. B., Velicogna, I., Gasson, E., Gomez, N., et al. (2021). The Paris Climate Agreement and future sea-level rise from Antarctica. *Nature*, *593*(7857), 83–89. https://doi.org/10.1038/s41586-021-03427-0

Diffenbaugh, N. S., & Barnes, E. A. (2023). Data-driven predictions of the time remaining until critical global warming thresholds are reached. *Proceedings of the National Academy of Sciences of the United States of America*, *120*(6), e2207183120. https://doi.org/10.1073/pnas.2207183120

Ding, Q., Steig, E. J., Battisti, D. S., & Küttel, M. (2011). Winter warming in West Antarctica caused by central tropical Pacific warming. *Nature Geoscience*, *4*(6), 398–403. https://doi.org/10.1038/ngeo1129

Dinniman, M. S., Klinck, J. M., & Smith, W. O. (2011). A model study of Circumpolar Deep Water on the West Antarctic Peninsula and Ross Sea continental shelves. *Deep Sea Research Part II: Topical Studies in Oceanography*, *58*(13–16), 1508–1523. https://doi.org/10.1016/J.DSR2.2010.11.013

Donat-Magnin, M., Jourdain, N. C., Spence, P., Le Sommer, J., Gallée, H., & Durand, G. (2017). Ice-shelf melt response to changing winds and glacier dynamics in the Amundsen Sea sector, Antarctica. *Journal of Geophysical Research: Oceans*, *122*(12), 10206–10224. https://doi.org/10.1002/2017JC013059

Dotto, T. S., Naveira Garabato, A. C., Wåhlin, A. K., Bacon, S., Holland, P. R., Kimura, S., et al. (2020). Control of the oceanic heat content of the Getz-Dotson Trough, Antarctica, by the Amundsen Sea Low. *Journal of Geophysical Research: Oceans*, *125*(8), e2020JC016113. https://doi.org/10.1029/2020JC016113

Edwards, T., Brandon, M. A., Durand, G., Edwards, N. R., Golledge, N. R., Holden, P. B., et al. (2019). Revisiting Antarctic ice loss due to marine ice-cliff instability. *Nature*, *566*(7742), 58–64. https://doi.org/10.1038/s41586-019-0901-4

Espinoza, V., Waliser, D. E., Guan, B., Lavers, D. A., & Ralph, F. M. (2018). Global analysis of climate change projection effects on atmospheric rivers. *Geophysical Research Letters*, *45*(9), 4299–4308. https://doi.org/10.1029/2017GL076968

Fasullo, J. T., & Richter, J. H. (2023). Dependence of strategic solar climate intervention on background scenario and model physics. *Atmospheric Chemistry and Physics*, *23*(1), 163–182. https://doi.org/10.5194/ACP-23-163-2023

Favier, L., Durand, G., Cornford, S. L., Gudmundsson, G. H., Gagliardini, O., Gillet-Chaulet, F., et al. (2014). Retreat of Pine Island Glacier controlled by marine ice-sheet instability. *Nature Climate Change*, *4*(2), 117–121. https://doi.org/10.1038/nclimate2094

Feldmann, J., & Levermann, A. (2015). Collapse of the West Antarctic Ice Sheet after local destabilization of the Amundsen Basin. *Proceedings of the National Academy of Sciences of the United States of America*, *112*(46), 14191–14196. https://doi.org/10.1073/PNAS.1512482112

Garbe, J., Albrecht, T., Levermann, A., Donges, J. F., & Winkelmann, R. (2020). The hysteresis of the Antarctic Ice Sheet. *Nature*, *585*(7826), 538–544. https://doi.org/10.1038/s41586-020-2727-5

Gettelman, A., Mills, M. J., Kinnison, D. E., Garcia, R. R., Smith, A. K., Marsh, D. R., et al. (2019). The Whole Atmosphere Community Climate Model Version 6 (WACCM6). *Journal of Geophysical Research: Atmospheres*, *124*(23), 12380–12403. https://doi.org/10.1029/2019JD030943

Goddard, P. B. (2023a). Data and Code for Goddard et al 2023 – SAI and Antarctica (1) [Computational Notebook & Dataset]. Zenodo. https://doi.org/10.5281/zenodo.8326651

Goddard, P. B. (2023b). Data and Code for Goddard et al 2023 – SAI and Antarctica (2) [Dataset]. Zenodo. https://doi.org/10.5281/zenodo.8327098

Goddard, P. B. (2023c). Data and Code for Goddard et al 2023 – SAI and Antarctica (3) [Dataset]. Zenodo. https://doi.org/10.5281/zenodo.8327136

Goddard, P. B. (2023d). Data and Code for Goddard et al 2023 – SAI and Antarctica (4) [Dataset]. Zenodo. https://doi.org/10.5281/zenodo.8327170
Goddard, P. B. (2023e). Data and Code for Goddard et al 2023 – SAI and Antarctica (5) [Dataset]. Zenodo. https://doi.org/10.5281/zenodo.8327176
Goddard, P. B., Dufour, C. O., Yin, J., Griffies, S. M., & Winton, M. (2017). CO_2-induced ocean warming of the Antarctic Continental Shelf in an Eddying Global Climate Model. *Journal of Geophysical Research: Oceans*, *122*(10), 8079–8101. https://doi.org/10.1002/2017JC012849
Goddard, P. B., Tabor, C. R., & Jones, T. R. (2021). Utilizing ice core and climate model data to understand seasonal west Antarctic variability. *Journal of Climate*, *34*(24), 10007–10026. https://doi.org/10.1175/JCLI-D-20-0822.1
Golledge, N., Keller, E. D., Gomez, N., Naughten, K. A., Bernales, J., Trusel, L. D., & Edwards, T. (2019). Global environmental consequences of twenty-first-century ice-sheet melt. *Nature*, *566*(7742), 65–72. https://doi.org/10.1038/s41586-019-0889-9
Gong, D., & Wang, S. (1999). Definition of Antarctic Oscillation index. *Geophysical Research Letters*, *26*(4), 459–462. https://doi.org/10.1029/1999GL900003
Greenbaum, J. S., Blankenship, D. D., Young, D. A., Richter, T. G., Roberts, J. L., Aitken, A. R. A., et al. (2015). Ocean access to a cavity beneath Totten Glacier in East Antarctica. *Nature Geoscience*, *8*(4), 294–298. https://doi.org/10.1038/ngeo2388
Hellmer, H. H., Kauker, F., Timmermann, R., Determann, J., & Rae, J. (2012). Twenty-first-century warming of a large Antarctic ice-shelf cavity by a redirected coastal current. *Nature*, *485*(7397), 225–228. https://doi.org/10.1038/nature11064
Herraiz-Borreguero, L., Coleman, R., Allison, I., Rintoul, S. R., Craven, M., & Williams, G. D. (2015). Circulation of modified Circumpolar Deep Water and basal melt beneath the Amery Ice Shelf, East Antarctica. *Journal of Geophysical Research: Oceans*, *120*(4), 3098–3112. https://doi.org/10.1002/2015JC010697
Herraiz-Borreguero, L., & Naveira Garabato, A. C. (2022). Poleward shift of Circumpolar Deep Water threatens the East Antarctic Ice Sheet. *Nature Climate Change*, *12*(8), 728–734. https://doi.org/10.1038/s41558-022-01424-3
Holland, P. R., Bracegirdle, T. J., Dutrieux, P., Jenkins, A., & Steig, E. J. (2019). West Antarctic ice loss influenced by internal climate variability and anthropogenic forcing. *Nature Geoscience*, *12*(9), 718–724. https://doi.org/10.1038/s41561-019-0420-9
Hosking, J. S., Orr, A., Bracegirdle, T. J., & Turner, J. (2016). Future circulation changes off West Antarctica: Sensitivity of the Amundsen Sea Low to projected anthropogenic forcing. *Geophysical Research Letters*, *43*(1), 367–376. https://doi.org/10.1002/2015GL067143
Hosking, J. S., Orr, A., Marshall, G. J., Turner, J., & Phillips, T. (2013). The influence of the Amundsen–Bellingshausen Seas low on the climate of West Antarctica and its representation in coupled climate model simulations. *Journal of Climate*, *26*(17), 6633–6648. https://doi.org/10.1175/JCLI-D-12-00813.1
Hughes, T. (1973). Is the West Antarctic Ice Sheet disintegrating? *Journal of Geophysical Research*, *78*(33), 7884–7910. https://doi.org/10.1029/JC078I033P07884
Iizuka, M., Seki, O., Wilson, D. J., Suganuma, Y., Horikawa, K., van de Flierdt, T., et al. (2023). Multiple episodes of ice loss from the Wilkes Subglacial Basin during the Last Interglacial. *Nature Communications*, *14*(1), 1–10. https://doi.org/10.1038/s41467-023-37325-y
IPCC. (2019). In H.-O. Pörtner, D. C. Roberts, V. Masson-Delmotte, P. Zhai, M. Tignor, E. Poloczanska, et al. (Eds.), *IPCC Special Report on the Ocean and Cryosphere in a Changing Climate*. In press.
Jacobs, S. S. (1991). On the nature and significance of the Antarctic Slope Front. *Marine Chemistry*, *35*(1–4), 9–24. https://doi.org/10.1016/S0304-4203(09)90005-6
Jacobs, S. S., Hellmer, H. H., & Jenkins, A. (1996). Antarctic ice sheet melting in the Southeast Pacific. *Geophysical Research Letters*, *23*(9), 957–960. https://doi.org/10.1029/96GL00723
Jenkins, A., & Jacobs, S. (2008). Circulation and melting beneath George VI Ice Shelf, Antarctica. *Journal of Geophysical Research*, *113*(C4), 4013. https://doi.org/10.1029/2007JC004449
Johnson, A., Hock, R., & Fahnestock, M. (2022). Spatial variability and regional trends of Antarctic ice shelf surface melt duration over 1979–2020 derived from passive microwave data. *Journal of Glaciology*, *68*(269), 533–546. https://doi.org/10.1017/JOG.2021.112
Joughin, I., Smith, B. E., & Medley, B. (2014). Marine ice sheet collapse potentially under way for the thwaites glacier basin, West Antarctica. *Science*, *344*(6185), 735–738. https://doi.org/10.1126/SCIENCE.1249055
Kidson, J. W. (1988). Interannual variations in the Southern Hemisphere circulation. *Journal of Climate*, *1*(12), 1177–1198. https://doi.org/10.1175/1520-0442(1988)001<1177:ivitsh>2.0.co;2
Kravitz, B., Macmartin, D. G., Mills, M. J., Richter, J. H., Tilmes, S., Lamarque, J. F., et al. (2017). First simulations of designing stratospheric sulfate aerosol geoengineering to meet multiple simultaneous climate objectives. *Journal of Geophysical Research: Atmospheres*, *122*(23), 12616–12634. https://doi.org/10.1002/2017JD026874
Kravitz, B., MacMartin, D. G., Wang, H., & Rasch, P. J. (2016). Geoengineering as a design problem. *Earth System Dynamics*, *7*(2), 469–497. https://doi.org/10.5194/esd-7-469-2016
Lawrence, D. M., Fisher, R. A., Koven, C. D., Oleson, K. W., Swenson, S. C., Bonan, G., et al. (2019). The Community Land Model Version 5: Description of new features, benchmarking, and impact of forcing uncertainty. *Journal of Advances in Modeling Earth Systems*, *11*(12), 4245–4287. https://doi.org/10.1029/2018MS001583
Lee, W. R., MacMartin, D. G., Visioni, D., & Kravitz, B. (2021). High-latitude stratospheric aerosol geoengineering can be more effective if injection is limited to spring. *Geophysical Research Letters*, *48*(9), e2021GL092696. https://doi.org/10.1029/2021GL092696
Lee, W. R., MacMartin, D. G., Visioni, D., Kravitz, B., Chen, Y., Moore, J. C., et al. (2023). High-latitude stratospheric aerosol injection to preserve the Arctic. *Earth's Future*, *11*(1), e2022EF003052. https://doi.org/10.1029/2022EF003052
Liu, X., Ma, P. L., Wang, H., Tilmes, S., Singh, B., Easter, R. C., et al. (2016). Description and evaluation of a new four-mode version of the Modal Aerosol Module (MAM4) within version 5.3 of the Community Atmosphere Model. *Geoscientific Model Development*, *9*(2), 505–522. https://doi.org/10.5194/GMD-9-505-2016
Maclennan, M. L., & Lenaerts, J. T. M. (2021). Large-scale atmospheric drivers of snowfall over Thwaites Glacier, Antarctica. *Geophysical Research Letters*, *48*(17), e2021GL093644. https://doi.org/10.1029/2021GL093644
MacMartin, D. G., Visioni, D., Kravitz, B., Richter, J. H., Felgenhauer, T., Lee, W. R., et al. (2022). Scenarios for modeling solar radiation modification. *Proceedings of the National Academy of Sciences*, *119*(33), e2202230119. https://doi.org/10.1073/PNAS.2202230119
Marshall, G. J. (2003). Trends in the Southern Annular Mode from observations and reanalyses. *Journal of Climate*, *16*(24), 4134–4143. https://doi.org/10.1175/1520-0442(2003)016<4134:TITSAM>2.0.CO;2
McCusker, K. E., Battisti, D. S., & Bitz, C. M. (2015). Inability of stratospheric sulfate aerosol injections to preserve the West Antarctic Ice Sheet. *Geophysical Research Letters*, *42*(12), 4989–4997. https://doi.org/10.1002/2015GL064314
McKay, D. I. A., Staal, A., Abrams, J. F., Winkelmann, R., Sakschewski, B., Loriani, S., et al. (2022). Exceeding 1.5°C global warming could trigger multiple climate tipping points. *Science*, *377*(6611), eabn7950. https://doi.org/10.1126/science.abn7950
Meinshausen, M., Nicholls, Z. R. J., Lewis, J., Gidden, M. J., Vogel, E., Freund, M., et al. (2020). The shared socio-economic pathway (SSP) greenhouse gas concentrations and their extensions to 2500. *Geoscientific Model Development*, *13*(8), 3571–3605. https://doi.org/10.5194/GMD-13-3571-2020

Mo, K. C., & Higgins, R. W. (1998). The Pacific-South American modes and tropical convection during the Southern Hemisphere winter. *Monthly Weather Review*, *126*(6), 1581–1596. https://doi.org/10.1175/1520-0493(1998)126<1581:TPSAMA>2.0.CO;2

Moore, J. C., Rinke, A., Yu, X., Ji, D., Cui, X., Li, Y., et al. (2014). Arctic sea ice and atmospheric circulation under the GeoMIP G1 scenario. *Journal of Geophysical Research: Atmospheres*, *119*(2), 567–583. https://doi.org/10.1002/2013JD021060

Moorman, R., Morrison, A. K., & Hogg, A. M. C. (2020). Thermal responses to Antarctic ice shelf melt in an eddy-rich global ocean–sea ice model. *Journal of Climate*, *33*(15), 6599–6620. https://doi.org/10.1175/JCLI-D-19-0846.1

O'Brien, T. A., Wehner, M. F., Payne, A. E., Shields, C. A., Rutz, J. J., Leung, L. R., et al. (2022). Increases in future AR count and size: Overview of the ARTMIP Tier 2 CMIP5/6 experiment. *Journal of Geophysical Research: Atmospheres*, *127*(6), e2021JD036013. https://doi.org/10.1029/2021JD036013

Palóczy, A., Gille, S. T., & McClean, J. L. (2018). Oceanic heat delivery to the Antarctic continental shelf: Large-scale, low-frequency variability. *Journal of Geophysical Research: Oceans*, *123*(11), 7678–7701. https://doi.org/10.1029/2018JC014345

Payne, A. E., Demory, M. E., Leung, L. R., Ramos, A. M., Shields, C. A., Rutz, J. J., et al. (2020). Responses and impacts of atmospheric rivers to climate change. *Nature Reviews Earth & Environment*, *1*(3), 143–157. https://doi.org/10.1038/s43017-020-0030-5

Payne, A. J., Nowicki, S., Abe-Ouchi, A., Agosta, C., Alexander, P., Albrecht, T., et al. (2021). Future sea level change under coupled model intercomparison project phase 5 and phase 6 scenarios from the Greenland and Antarctic ice sheets. *Geophysical Research Letters*, *48*(16), e2020GL091741. https://doi.org/10.1029/2020GL091741

Perlwitz, J. (2011). Tug of war on the jet stream. *Nature Climate Change*, *1*(1), 29–31. https://doi.org/10.1038/nclimate1065

Raphael, M. N., Marshall, G. J., Turner, J., Fogt, R. L., Schneider, D., Dixon, D. A., et al. (2016). The Amundsen Sea low: Variability, change, and impact on Antarctic climate. *Bulletin of the American Meteorological Society*, *97*(1), 111–121. https://doi.org/10.1175/BAMS-D-14-00018.1

Ribeiro, N., Herraiz-Borreguero, L., Rintoul, S. R., McMahon, C. R., Hindell, M., Harcourt, R., & Williams, G. (2021). Warm modified circumpolar deep water intrusions drive ice shelf melt and inhibit dense shelf water formation in Vincennes Bay, East Antarctica. *Journal of Geophysical Research: Oceans*, *126*(8), e2020JC016998. https://doi.org/10.1029/2020JC016998

Rignot, E., Mouginot, J., Morlighem, M., Seroussi, H., & Scheuchl, B. (2014). Widespread, rapid grounding line retreat of Pine Island, Thwaites, Smith, and Kohler glaciers, West Antarctica, from 1992 to 2011. *Geophysical Research Letters*, *41*(10), 3502–3509. https://doi.org/10.1002/2014GL060140

Rignot, E., Mouginot, J., Scheuchl, B., Van Den Broeke, M., Van Wessem, M. J., & Morlighem, M. (2019). Four decades of Antarctic ice sheet mass balance from 1979–2017. *Proceedings of the National Academy of Sciences of the United States of America*, *116*(4), 1095–1103. https://doi.org/10.1073/PNAS.1812883116

Ryan, S., Hellmer, H. H., Janout, M., Darelius, E., Vignes, L., & Schröder, M. (2020). Exceptionally warm and prolonged flow of Warm Deep Water toward the Filchner-Ronne Ice Shelf in 2017. *Geophysical Research Letters*, *47*(13), e2020GL088119. https://doi.org/10.1029/2020GL088119

Scambos, T., Fricker, H. A., Liu, C. C., Bohlander, J., Fastook, J., Sargent, A., et al. (2009). Ice shelf disintegration by plate bending and hydro-fracture: Satellite observations and model results of the 2008 Wilkins ice shelf break-ups. *Earth and Planetary Science Letters*, *280*(1–4), 51–60. https://doi.org/10.1016/J.EPSL.2008.12.027

Schlosser, E., Manning, K. W., Powers, J. G., Duda, M. G., Birnbaum, G., & Fujita, K. (2010). Characteristics of high-precipitation events in Dronning Maud Land, Antarctica. *Journal of Geophysical Research*, *115*(D14), 14107. https://doi.org/10.1029/2009JD013410

Schneider, D. P., Okumura, Y., & Deser, C. (2012). Observed Antarctic interannual climate variability and tropical linkages. *Journal of Climate*, *25*(12), 4048–4066. https://doi.org/10.1175/JCLI-D-11-00273.1

Schoof, C. (2007). Ice sheet grounding line dynamics: Steady states, stability, and hysteresis. *Journal of Geophysical Research*, *112*(F3), F03S28. https://doi.org/10.1029/2006JF000664

Scott, R. C., Nicolas, J. P., Bromwich, D. H., Norris, J. R., & Lubin, D. (2019). Meteorological drivers and large-scale climate forcing of West Antarctic surface melt. *Journal of Climate*, *32*(3), 665–684. https://doi.org/10.1175/JCLI-D-18-0233.1

Siahaan, A., Smith, R. S., Holland, P. R., Jenkins, A., Gregory, J. M., Lee, V., et al. (2022). The Antarctic contribution to 21st-century sea-level rise predicted by the UK Earth System Model with an interactive ice sheet. *Cryosphere*, *16*(10), 4053–4086. https://doi.org/10.5194/TC-16-4053-2022

Smith, B., Fricker, H. A., Gardner, A. S., Medley, B., Nilsson, J., Paolo Nicholas Holschuh, F. S., et al. (2020). Pervasive ice sheet mass loss reflects competing ocean and atmosphere processes. *Science*, *368*(6496), 1239–1242. https://doi.org/10.1126/science.aaz5845

Smith, R., Jones, P., Briegleb, B., Bryan, F., Danabasoglu, G., Dennis, J., et al. (2010). The parallel ocean program (POP) reference manual, ocean component of the community climate system model (CCSM). *LANL Technical Report, LAUR-10-01853*, 141.

Sparrow, M., Chapman, P., & Gould, J. (Eds.). (2011). *2005 The World Ocean Circulation Experiment (WOCE) Hydrographic Atlas Series (4 volumes)*. International WOCE Project Office.

Spence, P., Griffies, S. M., England, M. H., Hogg, A. M. C., Saenko, O. A., & Jourdain, N. C. (2014). Rapid subsurface warming and circulation changes of Antarctic coastal waters by poleward shifting winds. *Geophysical Research Letters*, *41*(13), 4601–4610. https://doi.org/10.1002/2014GL060613

Steig, E. J., Ding, Q., Battisti, D. S., & Jenkins, A. (2012). Tropical forcing of Circumpolar Deep Water inflow and outlet glacier thinning in the Amundsen Sea Embayment, West Antarctica. *Annals of Glaciology*, *53*(60), 19–28. https://doi.org/10.3189/2012AoG60A110

Stewart, A. L., Klocker, A., & Menemenlis, D. (2018). Circum-Antarctic shoreward heat transport derived from an eddy- and tide-resolving simulation. *Geophysical Research Letters*, *45*(2), 834–845. https://doi.org/10.1002/2017GL075677

Stewart, A. L., & Thompson, A. F. (2015). Eddy-mediated transport of warm Circumpolar Deep Water across the Antarctic Shelf Break. *Geophysical Research Letters*, *42*(2), 432–440. https://doi.org/10.1002/2014GL062281

Sutter, J., Jones, A., Frölicher, T. L., Wirths, C., & Stocker, T. F. (2023). Climate intervention on a high-emissions pathway could delay but not prevent West Antarctic Ice Sheet demise. *Nature Climate Change*, *13*(9), 951–960. https://doi.org/10.1038/s41558-023-01738-w

Thoma, M., Jenkins, A., Holland, D., & Jacobs, S. (2008). Modelling Circumpolar Deep Water intrusions on the Amundsen Sea continental shelf, Antarctica. *Geophysical Research Letters*, *35*(18), L18602. https://doi.org/10.1029/2008GL034939

Thompson, A. F., Heywood, K. J., Schmidtko, S., & Stewart, A. L. (2014). Eddy transport as a key component of the Antarctic overturning circulation. *Nature Geoscience*, *7*(12), 879–884. https://doi.org/10.1038/ngeo2289

Thompson, D. W. J., Solomon, S., Kushner, P. J., England, M. H., Grise, K. M., & Karoly, D. J. (2011). Signatures of the Antarctic ozone hole in Southern Hemisphere surface climate change. *Nature Geoscience*, *4*(11), 741–749. https://doi.org/10.1038/ngeo1296

Tilmes, S., Fasullo, J., Lamarque, J. F., Marsh, D. R., Mills, M., Alterskjær, K., et al. (2013). The hydrological impact of geoengineering in the Geoengineering Model Intercomparison Project (GeoMIP). *Journal of Geophysical Research: Atmospheres*, *118*(19), 11036–11058. https://doi.org/10.1002/JGRD.50868

Tilmes, S., Richter, J. H., Kravitz, B., Macmartin, D. G., Mills, M. J., Simpson, I. R., et al. (2018). CESM1(WACCM) Stratospheric Aerosol Geoengineering Large Ensemble Project. *Bulletin of the American Meteorological Society*, *99*(11), 2361–2371. https://doi.org/10.1175/BAMS-D-17-0267.1

Tilmes, S., Richter, J. H., Mills, M. J., Kravitz, B., Macmartin, D. G., Vitt, F., et al. (2017). Sensitivity of aerosol distribution and climate response to stratospheric SO_2 injection locations. *Journal of Geophysical Research: Atmospheres*, *122*(23), 12591–12615. https://doi.org/10.1002/2017JD026888

Trusel, L. D., Frey, K. E., Das, S. B., Karnauskas, K. B., Kuipers Munneke, P., Van Meijgaard, E., & Van Den Broeke, M. R. (2015). Divergent trajectories of Antarctic surface melt under two twenty-first-century climate scenarios. *Nature Geoscience*, *8*(12), 927–932. https://doi.org/10.1038/ngeo2563

Turner, J., Bracegirdle, T. J., Phillips, T., Marshall, G. J., & Scott Hosking, J. (2013). An initial assessment of Antarctic sea ice extent in the CMIP5 models. *Journal of Climate*, *26*(5), 1473–1484. https://doi.org/10.1175/JCLI-D-12-00068.1

Turner, J., Phillips, T., Thamban, M., Rahaman, W., Marshall, G. J., Wille, J. D., et al. (2019). The dominant role of extreme precipitation events in Antarctic snowfall variability. *Geophysical Research Letters*, *46*(6), 3502–3511. https://doi.org/10.1029/2018GL081517

van Angelen, J. H., van den Broeke, M. R., Wouters, B., & Lenaerts, J. T. M. (2014). Contemporary (1960–2012) evolution of the climate and surface mass balance of the Greenland ice sheet. *Surveys in Geophysics*, *35*(5), 1155–1174. https://doi.org/10.1007/S10712-013-9261-Z/FIGURES/13

Verfaillie, D., Pelletier, C., Goosse, H., Jourdain, N. C., Bull, C. Y. S., Dalaiden, Q., et al. (2022). The circum-Antarctic ice-shelves respond to a more positive Southern Annular Mode with regionally varied melting. *Communications Earth & Environment*, *3*, 139. https://doi.org/10.1038/s43247-022-00458-x

Visioni, D., Bednarz, E. M., MacMartin, D. G., Kravitz, B., & Goddard, P. B. (2023). The choice of baseline period influences the assessments of the outcomes of stratospheric aerosol injection. *Earth's Future*, *11*(8), e2023EF003851. https://doi.org/10.1029/2023EF003851

Visioni, D., MacMartin, D. G., Kravitz, B., Richter, J. H., Tilmes, S., & Mills, M. J. (2020). Seasonally modulated stratospheric aerosol geoengineering alters the climate outcomes. *Geophysical Research Letters*, *47*(12), e2020GL088337. https://doi.org/10.1029/2020GL088337

Weertman, J. (1974). Stability of the junction of an ice sheet and an ice shelf. *Journal of Glaciology*, *13*(67), 3–11. https://doi.org/10.3189/S0022143000023327

Whitworth, T., Orsi, A. H., Kim, S. J., Nowlin, W. D., & Locarnini, R. A. (1998). Water masses and mixing near the Antarctic Slope Front. In S. S. Jacobs & R. F. Weiss (Eds.), *Ocean, ice, and atmosphere: Interactions at the Antarctic continental margins*, *Antarctic Research Series* (Vol. 75, pp. 1–27). AGU. https://doi.org/10.1029/AR075p0001

Wilks, D. S. (1997). Resampling hypothesis tests for autocorrelated fields. *Journal of Climate*, *10*(1), 65–83. https://doi.org/10.1175/1520-0442(1997)010<0065:RHTFAF>2.0.CO;2

Wille, J. D., Favier, V., Gorodetskaya, I. V., Agosta, C., Kittel, C., Beeman, J. C., et al. (2021). Antarctic atmospheric river climatology and precipitation impacts. *Journal of Geophysical Research: Atmospheres*, *126*(8), e2020JD033788. https://doi.org/10.1029/2020JD033788

Yamazaki, K., Aoki, S., Katsumata, K., Hirano, D., & Nakayama, Y. (2021). Multidecadal poleward shift of the southern boundary of the Antarctic Circumpolar Current off East Antarctica. *Science Advances*, *7*(24), 8755–8766. https://doi.org/10.1126/SCIADV.ABF8755

Yeung, Y., Yiu, S., & Maycock, A. C. (2019). On the seasonality of the El Niño Teleconnection to the Amundsen Sea Region. *Journal of Climate*, *32*(15), 4829–4845. https://doi.org/10.1175/JCLI-D-18-0813.1

Yu, H., Rignot, E., Seroussi, H., Morlighem, M., & Choi, Y. (2019). Impact of iceberg calving on the retreat of Thwaites Glacier, West Antarctica over the next century with different calving laws and ocean thermal forcing. *Geophysical Research Letters*, *46*(24), 14539–14547. https://doi.org/10.1029/2019GL084066

Yu, L., Zhang, Z., Zhou, M., Zhong, S., Lenschow, D., Hsu, H., et al. (2012). Influence of the Antarctic Oscillation, the Pacific–South American modes and the El Niño–Southern Oscillation on the Antarctic surface temperature and pressure variations. *Antarctic Science*, *24*(1), 59–76. https://doi.org/10.1017/S095410201100054X

Zhang, Y., MacMartin, D. G., Visioni, D., Bednarz, E., & Kravitz, B. (2023). Introducing a comprehensive set of stratospheric aerosol injection strategies. EGUsphere. [preprint]. https://doi.org/10.5194/egusphere-2023-117

Zheng, F., Li, J., Clark, R. T., & Nnamchi, H. C. (2013). Simulation and projection of the Southern Hemisphere annular mode in CMIP5 models. *Journal of Climate*, *26*(24), 9860–9879. https://doi.org/10.1175/JCLI-D-13-00204.1